Working title:

Voltage-gated Ca^{2+} and K^{+} channel coupling regulates CA1 hippocampal synaptic filtering and spine excitability

Authors:

Jonathan G. Murphy[1], Jakob J. Gutzmann[1], Lin Lin[1], Jiahua Hu[1], Ronald S. Petralia[2], Ya-Xian Wang[2], and Dax A. Hoffman[1]

Affiliations:

[1]*Eunice Kennedy Shriver* National Institute of Child Health and Human Development and [2]Advanced Imaging Core, National Institute on Deafness and Other Communication Disorders, National Institutes of Health, Bethesda, MD

ABSTRACT

The transient voltage-gated K^{+} current (I_A) mediated by Kv4.2 in CA1 hippocampal pyramidal neurons regulates dendritic excitability, synaptic plasticity, and learning. Here we report that Ca^{2+} entry mediated by the voltage-gated Ca^{2+} channel subunit Cav2.3 regulates Kv4.2 function in CA1 pyramidal neurons through Ca^{2+} binding auxiliary subunits known as K^{+} channel interacting proteins (KChIPs). We characterized an interaction between Cav2.3 and Kv4.2 using immunofluorescence colocalization, coimmunoprecipitation, electron microscopy, FRAP, and FRET. We found that Ca^{2+}-entry via Cav2.3 increases Kv4.2-mediated whole-cell current due in part to an increase in Kv4.2 surface expression. In hippocampal neurons, pharmacological block of Cav2.3 reduced whole-cell I_A. We also found reduced I_A in Cav2.3 knockout mouse neurons with a loss of the dendritic I_A gradient. Furthermore, the Cav2.3-Kv4.2 complex was found to regulate the size of synaptic currents and spine Ca^{2+} transients. These results reveal an intermolecular Cav2.3-Kv4.2 complex impacting synaptic integration in CA1 hippocampal neurons.

INTRODUCTION

In neuronal dendrites, voltage-gated ion channels modulate the amplitude, propagation and integration of synaptic input. The voltage-gated K^+ channel subunit Kv4.2 is highly expressed in the dendrites of hippocampal CA1 pyramidal neurons where it assembles into tetrameric channels that conduct a subthreshold-activated transient outward K^+ current known as A-type current (I_A) (1-5). Dendritic I_A regulates neuronal excitability by opposing depolarization to filter synaptic input, dampen the magnitude of backpropagating action potentials (bAP), oppose dendritic plateau potentials, and limit the size of glutamate uncaging evoked spine Ca^{2+} entry (5-11). As a consequence, the primary A-type channel expressed in CA1 pyramidal neuron dendrites, Kv4.2, plays an active role in shaping propagation of synaptic input, hippocampal synaptic plasticity, and learning (5, 8, 12-18). Dysregulation of I_A has been reported in both animal models and human cases of Alzheimer's disease, epilepsy, and pain sensitization (19-26). A better understanding of the mechanisms underlying neuronal I_A would facilitate the identification of therapeutic targets.

The properties of neuronal I_A can only be recapitulated in heterologous systems by expression of auxiliary subunits known as K^+ channel interacting proteins (KChIPs) and dipeptidyl aminopeptidase-like proteins (DPPs), which have profound effects on Kv4 subunit expression, stability, and biophysical properties (27-30). KChIPs are small (188-285 aa) Ca^{2+}-binding proteins of the neuronal Ca^{2+} sensor (NCS) gene family expressed from four genes (*KCNIP1-4*). KChIPs are highly conserved in their globular core domain (~70%) that contains N and C lobules, each with two EF-hands (EF) surrounding a deep hydrophobic pocket that cradles the N-terminus of the Kv4 subunit (31-33). Like the other NCS proteins, KChIP EFs 2, 3 and 4 bind divalent metal ions whereas EF1 is degenerated such that it cannot (34). At physiological free Ca^{2+} concentrations in neurons, the Ca^{2+} occupancy at the three Ca^{2+}-binding EF-hands is unknown. However, dynamic Ca^{2+} binding in response to transient Ca^{2+} elevations during neuronal activity could provide a regulatory feedback mechanism onto Kv4 channels. Interestingly, Ca^{2+} binding to purified KChIP induces global structural changes throughout the protein that may regulate oligomerization and Kv4 interactions (35-39). The effects of Ca^{2+} on the Kv4-KChIP complex has been studied using EF-hand mutations or by altering intracellular free Ca^{2+} concentrations (27, 31, 40-42). However, while EF-hand mutations potently reduce KChIP regulation of Kv4 channel trafficking and function, they are likely to disrupt the tertiary structure of the protein independent of Ca^{2+} (43). Furthermore, patch clamp studies of Kv4 channel function in various neuronal and non-neuronal cell types by addition of intracellular free Ca^{2+} or Ca^{2+} chelators in the patch pipette

have been variable and difficult to interpret (41, 44-46). In a similar effort to test the role of elevated intracellular Ca^{2+} on Kv4-KChIP function, we recently reported an increase in Kv4.2 current density when intracellular free Ca^{2+} was clamped at ~10 μM using a low affinity Ca^{2+} chelator (HEDTA) in the patch pipette in HEK293T cell recordings (42). This effect was unique to a subset of KChIP isoforms suggesting that cell-type specific KChIP expression may be an under-appreciated aspect of Ca^{2+} regulation of Kv4-KChIP complexes.

In neurons, it is well known that Ca^{2+} activated K^+ channels (KCa) rely on voltage-gated Ca^{2+} entry to repolarize the plasma membrane (47). However, the canonically voltage-activated Kv4 channels have also been reported to be targets of voltage-gated Ca^{2+} channel (VGCC) regulation through KChIP auxiliary subunits. Cerebellar stellate cells, small inhibitory interneurons that modulate Purkinje cell output, express Kv4-mediated I_A that is regulated by Ca^{2+} entry through low-threshold T-type voltage-gated Ca^{2+} channels (Cav3). T-type channel block with the L- and T-type channel-selective drug mibefradil increases the availability of I_A at more negative membrane potentials (48, 49). This effect was blocked by intracellular dialysis of BAPTA or pan-KChIP antibody consistent with a Kv4, Cav3, and KChIP complex.

In hippocampal CA1 pyramidal neurons, Wang and colleagues reported that Cav2.3 (R-type) voltage-gated Ca^{2+} channels function to attenuate the size of evoked EPSPs by boosting Kv4 channel function (50). Cav2.3 channels are expressed in the dendrites and spines of CA1 hippocampal pyramidal neurons and regulate action potential afterhyperpolarization and afterdepolarization, the magnitude of bAP evoked Ca^{2+} transients, and Ca^{2+} influx in spines and dendrites (51-57). Wang et al. disrupted Cav2.3 regulation of Kv4 using BAPTA or a pan-KChIP antibody in the patch pipette suggesting Cav2.3, Kv4, and KChIP are in close proximity (<50 nm). However, the studies by Wang and colleagues did not describe the nature of the Cav2.3-Kv4 interaction, nor the effect of Cav2.3-mediated Ca^{2+} entry on I_A. In the current study we corroborate and expand on the findings of Wang et al. by identifying a nanoscale interaction between Cav2.3 and Kv4.2 that regulates Kv4.2 function by a novel mechanism.

102 RESULTS

103

104 **Cav2.3 and Kv4.2 form an ion channel complex in hippocampal neurons**

105 The characteristic kinetics of neuronal I_A requires expression of KChIP and DPP
106 accessory subunits that had been identified and described nearly two decades ago (27, 28). In
107 an effort to identify novel Kv4.2 protein interactions and modifying enzymes in hippocampal
108 neurons we used tandem affinity purification (TAP) and protein identification with mass
109 spectrometry (MS) (58). As expected, Kv4.2 pulled down Kv4.1, Kv4.2, Kv4.3, and previously
110 described auxiliary subunits (DPPs and KChIPs) confirming the specificity of the assay (**Figure 1**
111 **– Figure supplement 1A**). In addition to known binding partners, we also identified peptides
112 representing a significant proportion of the Cav2.3 amino acid sequence (**Figure 1 – Figure**
113 **supplement 1B,C**). Cav2.3 was the only voltage-gated Ca^{2+} channel identified in this screen.

114 To confirm the presence of a hippocampal Cav2.3 and Kv4.2 molecular complex we
115 carried out several immunological measurements using hippocampal tissue. Broad neuropil
116 colocalization of endogenous Cav2.3 and Kv4.2 immunofluorescent signal was consistent with
117 enrichment in the dendrite layers of the hippocampus as has been previously reported for each
118 channel separately (**Figure 1A**) (51, 59). Both Cav2.3 and Kv4.2 are also known to be expressed
119 in dendrites and spines. To evaluate Cav2.3-Kv4.2 colocalization, we transfected cultured
120 hippocampal neurons with Cav2.3-GFP (i), Kv4.2-myc (ii), and mCherry (iii) plasmids (**Figure 1B**).
121 In addition to immunofluorescent colocalization in dendrites, both channels were enriched in
122 spines when compared to the free cytosolic mCherry fluorescent protein (**Figure 1C,D**).
123 Immunofluorescent overlap suggests that Cav2.3-Kv4.2 complexes may exist in dendritic spines,
124 but, due to a lack of clear punctate signal we measured colocalization with greater precision using
125 double immunogold electron microscopy. Gold particle labeling of Cav2.3 and Kv4.2 is visible
126 near synapses in dendritic spines and we found evidence of colocalization both near the post
127 synaptic density (**Figure 1Ei**) and in the spine head (**Figure 1Eii**). We further confirmed the
128 Cav2.3-Kv4.2 complex by co-immunoprecipitation of native Kv4.2 after Cav2.3 pulldown in lysates
129 from WT hippocampal tissue, but not Cav2.3 knockout (KO), confirming the specificity of the anti-
130 Cav2.3 antibody (**Figure 1F**).

131

132 **Cav2.3 regulates Kv4.2 mobility in HEK293FT cells and neuronal dendrites**

133 If Cav2.3 and Kv4.2 bind, we reasoned that assembly of such a high molecular weight
134 plasma membrane complex would result in a decrease in FRAP mobility. HEK293FT cells were
135 transfected with either YFP-Cav2.3 and CFP or Kv4.2-CFP and YFP and photobleaching was

136 performed in separate cells (**Figure 2A**). When expressed separately, YFP-Cav2.3 mobile
137 fraction (66.49 ± 0.01%) was considerably larger than Kv4.2-CFP (56.01 ± 0.09%) (**Figure 2B,E**).
138 Expression of YFP-Cav2.3 and Kv4.2-CFP in the same cell and simultaneous bleaching yielded
139 a decrease in mobile fraction for both YFP-Cav2.3 (56.28 ± 0.22%) and Kv4.2-CFP (36.77 ±
140 0.12%) suggesting that coexpression of Cav2.3 and Kv4.2 is sufficient to mediate a binding
141 interaction in non-neuronal cells (**Figure 2C,D,E**). In neurons, prominent immunolabel
142 colocalization led us to test whether Cav2.3 regulates Kv4.2 mobility in spines and dendrites.
143 Primary mouse neurons cultured from either WT or Cav2.3 KO mice were transfected with Kv4.2-
144 GFP and mCherry as a cell-fill to track dendrite structure during photobleaching recovery time-
145 courses for small sections of dendrite shafts or entire spines (**Figure 2F,H**). Kv4.2-GFP mobile
146 fraction was significantly higher in dendrites (55.96 ± 0.01%) when compared to spines (45.00 ±
147 0.02%) (**Figure 2G,I,J**). This result is consistent with the diffusion limit imposed by the spine neck
148 and previously reported Kv4.2 interactions with postsynaptic scaffold proteins including PSD95
149 (60, 61), SAP97 (62), and AKAP79/150 (63). Kv4.2-GFP mobile fraction was increased
150 specifically in dendrite shafts (+9.85 ± 3.21%) as opposed to spines (+6.45 ± 3.21%) of Cav2.3
151 KO mouse neurons (**Figure 2G,I,J**). This is likely due to the higher concentration of immobile
152 Kv4.2 binding partners in spines relative to dendrites that mask the effects of Cav2.3 binding. Our
153 FRAP results in both HEK293FT cells and cultured hippocampal neurons supports the hypothesis
154 that Cav2.3 and Kv4.2 form a protein complex that reduces free diffusion of Kv4.2 in living cells.
155

156 **Cav2.3 and Kv4.2 bind at a 1:1 ion channel stoichiometry within a cellular nanodomain**

157 After confirming a Cav2.3-Kv4.2 complex in hippocampal neurons, we next sought to
158 determine if Cav2.3 and Kv4.2 were within close enough proximity to each other to form a
159 functional Ca^{2+} nanodomain. FRET is a distance dependent physical process that involves the
160 non-radiative transfer of energy from an electronically excited donor to a nearby acceptor
161 fluorophore; FRET efficiency decays at the inverse sixth power of the distance between two
162 molecules (64). Using the CFP and YFP donor/acceptor pair, FRET can only be detected when
163 the distance between donor and acceptor is <10 nm (65). To determine if Kv4.2 and Cav2.3 were
164 within this distance we first introduced Kv4.2-CFP or YFP-Cav2.3 into HEK293FT cells with
165 soluble YFP or CFP respectively to confirm that FRET would not arise from non-specific protein-
166 protein interactions in the cell (0.68 ±0.34% and 0.46 ± 0.21%) (**Figure 3A,B**). To establish the
167 utility of our FRET system, we then coexpressed Kv4.2-YFP and KChIP3a-CFP, which, as
168 expected, yielded a high FRET efficiency (11.22 ± 0.57%). Coexpression of Kv4.2-CFP and YFP-
169 Cav2.3 also resulted in FRET (6.71 ± 0.39%), confirming that they bind within a 10 nm domain

170 (**Figure 3A,B**). Next, we sought to leverage the maximal FRET efficiencies obtained from donor
171 or acceptor-focused measurements to determine the stoichiometry of the Cav2.3-Kv4.2 complex
172 using the method of Ben-Johny and colleagues (66). This method relies on maximizing the FRET
173 signal at either the donor ($FRET_{D,MAX}$) or acceptor ($FRET_{A,MAX}$) with saturating concentrations of
174 free acceptors or donors. The stoichiometry of the FRET complex can be estimated based on the
175 maximal efficiency of interacting acceptors and donors and expressed as the stoichiometry ratio
176 ($FRET_{A,MAX}/FRET_{D,MAX}$). We validated this method in our hands by taking advantage of known
177 stoichiometries of Kv4.2 binding with KChIP (1:1) and A-kinase anchoring protein 79 (AKAP79)
178 binding with the regulatory subunit of protein kinase A, RIIα (1:2). After coexpressing varying
179 ratios of Kv4.2-YFP and KChIP3a-CFP we measured similar maximum FRET efficiencies at both
180 donor and acceptor ($FRET_{A,MAX}$: 15.98 $\pm$ 0.64%; $FRET_{D,MAX}$: 15.75 $\pm$ 0.79%) consistent with a
181 1:1 interaction (**Figure 3C,F,G**). For AKAP79-YFP and PKA-RII-CFP we measured maximum
182 FRET efficiencies that were most consistent with the expected 1:2 stoichiometry ($FRET_{A,MAX}$:
183 13.28 $\pm$ 1.13%; $FRET_{D,MAX}$: 5.35 $\pm$ 0.26%) (**Figure 3D,F,G**). Determination of the stoichiometry
184 of YFP-Cav2.3 and Kv4.2-CFP indicated that the FRET complex was most consistent with a 1:4
185 acceptor:donor ratio that would be expected for a complex containing a single YFP-Cav2.3 α1
186 subunit and a Kv4.2-CFP homotetrameric channel ($FRET_{A,MAX}$: 14.52 $\pm$ 1.14%; $FRET_{D,MAX}$: 3.43
187 $\pm$ 0.33%) (**Figure 3E,F,G**). The results from our FRET experiments confirm that Cav2.3 and Kv4.2
188 are in close enough proximity to form a functional Ca^{2+} nanodomain (67, 68).
189
190 **Cav2.3 expression increases Kv4.2 current density in a KChIP- and Ca^{2+}-dependent**
191 **manner in HEK293FT cells.**
192 Cav2.3 and Kv4.2 binding led us to hypothesize that Cav2.3 may act as a local neuronal
193 Ca^{2+} source for Kv4.2 that can elevate nanodomain Ca^{2+} concentrations in the μM range. We
194 previously reported that ~10 μM intracellular free Ca^{2+} increased Kv4 current density when
195 expressed with a subset of KChIP isoforms including KChIP2b, KChIP2c, and KChIP3a (42). To
196 determine if Cav2.3 could serve as a Kv4.2 Ca^{2+} source, we expressed either Kv4.2 alone (**i**),
197 Kv4.2 and KChIP2c (**ii**), or Kv4.2, KChIP2c, and Cav2.3 (**iii**) (**Figure 4A**). As we and others have
198 previously described, KChIP2c increased Kv4.2 current density and slowed fast inactivation of
199 the macroscopic current (**Figure 4B,C**). Interestingly, coexpression of Cav2.3 significantly
200 elevated Kv4.2 current density (**Figure 4B,C**) without affecting other aspects of KChIP-dependent
201 regulation of Kv4.2 including voltage-dependence of inactivation and recovery from inactivation
202 (**Figure 4E,F**). We tested whether local Cav2.3-mediated Ca^{2+} influx led to increases Kv4.2

203 current by replacing EGTA in patch pipettes with intracellular solution containing the fast Ca^{2+}
204 chelator BAPTA. BAPTA blocked Cav2.3 increases in Kv4.2 current density (**Figure 4B,C**)
205 consistent with a nanodomain Ca^{2+} influx-mediated effect. Coexpression of a Ca^{2+}-dead KChIP2c
206 mutant, in which the Ca^{2+}-coordinating aspartate residue in position 1 of EF-hands 2, 3, and 4
207 was mutated to alanine, reversed the Cav2.3 effect (**Figure 4C**). Taken together, Cav2.3
208 expression caused a KChIP-dependent increase in Kv4.2 current density and required local
209 increases in free Ca^{2+}. As we observed no changes in Kv4.2 gating behavior by Cav2.3, the
210 increase in Kv4.2 current density may be explained by a change in channel surface localization.
211 To test this possibility, we transfected COS7 cells with Kv4.2 alone, Kv4.2 and Cav2.3, Kv4.2 and
212 KChIP2c, or Kv4.2, Cav2.3, and KChIP. We then surface labeled Kv4.2 with cell-impermeable
213 biotin and quantified the amount of surface Kv4.2 relative to total expression. Expression of
214 Cav2.3 with Kv4.2 and KChIP led to a significant increase in surface localization when compared
215 to Kv4.2 and KChIP alone (**Figure 4G,H**). The evidence provided so far suggests that when
216 Cav2.3 and Kv4.2 assemble in an ion channel signaling complex, Cav2.3-mediated Ca^{2+} entry
217 increases Kv4.2 surface localization in a KChIP-dependent manner.
218
219 **Cav2.3 sustains I_A in cultured hippocampal neurons.**
220 Armed with evidence that Cav2.3 and Kv4.2 colocalize in hippocampal neurons and that
221 Cav2.3 regulated Kv4.2 surface levels in heterologous cells, we wanted to determine if Cav2.3-
222 mediated Ca^{2+} entry regulates Kv4.2 function in neurons. The prominent dendritic localization of
223 Kv4 channels obscures accurate measurement of I_A using voltage clamp recordings from the
224 soma of developmentally mature neurons. However, at early developmental time points before
225 dendrite outgrowth and synaptic maturation, Kv4 channels would be predicted to be better
226 clamped (1). We found that somatic I_A density in cultured hippocampal neurons reaches a
227 maximum at 6-8 days in vitro (**Figure 5 – Figure Supplement 1A**). As the cultures mature, I_A
228 density drops dramatically as dendrites elaborate and excitatory synaptic development
229 progresses (**Figure 5 – Figure Supplement 1A,B**). Peak Cav2.3 current is elicited at membrane
230 potentials near 0 mV (69, 70). To maximize Cav2.3 channel activation we measured peak I_A in
231 DIV6-8 cultured neurons using voltage steps from -80 mV to 0 mV. Under these conditions, the
232 peak transient outward K^+ current was highly enriched for I_A relative to the slowly activating
233 delayed rectifier K^+ current (92.49 $\pm$ 0.02%; data not shown); therefore, we monitored total peak
234 outward current as a proxy for I_A. Voltage clamp recordings of I_A were stable over a 360 s
235 recording period (**Figure 5Ai,B,C**). We confirmed the presence of Kv4 channels in I_A recordings
236 by applying AmmTX3, a Kv4 selective scorpion toxin that requires the DPP auxiliary subunit for

237 high potency (**Figure 5Aii,B,C**) (71, 72). Ni^{2+}, a nonspecific VGCC blocker with high potency at
238 T- and R-type channels was applied to determine the effect of Cav2.3 on I_A (70, 73). Application
239 of Ni^{2+} to the bath led to a rapid dose-dependent reduction in I_A (**Figure 5Aiii,B,C,D**). IC_{50} of I_A
240 block (~44.1 μM) was within the reported IC_{50} range of Cav2.3 block by Ni^{2+} (27.4-66.0 μM) (74).
241 Ni^{2+} application did not shift I_A voltage dependence of inactivation as was previously reported for
242 Cav3 regulation of I_A in cerebellar stellate neurons (**Figure 5E**) (48, 49).
243
244 **I_A is reduced in Cav2.3 KO CA1 pyramidal neurons.**
245 To overcome the limitations of VGCC pharmacology, we measured I_A in the context of a
246 previously characterized Cav2.3 KO mouse (57, 75). Here, we made recordings from 6-8 weeks
247 old mouse CA1 pyramidal neurons. Unlike the DIV6-8 neurons used above, these neurons are
248 greater in size and express a more substantial proportion of contaminating delayed rectifier K^+
249 currents. Therefore, I_A was isolated as previously described using large voltage steps and
250 subtraction of the sustained outward current (I_{sus}) from the total outward current (I_{tot}) (**Figure 6A**)
251 (58). I_A was selectively reduced in whole-cell recordings from Cav2.3 KOs when compared to WT
252 mouse neurons while I_{sus} was unchanged (**Figure 6B**). Given the previously mentioned
253 complications with whole-cell voltage clamp, we pulled patches from the soma; however, outside-
254 out patches did not replicate the whole-cell reduction in I_A (**Figure 6C**). One explanation would be
255 if the whole-cell reduction in I_A we observed in Cav2.3 KO recordings arose from a specific loss
256 of dendritic Kv4.2 channels. To determine this, we performed cell-attached dendritic recordings
257 along the apical dendrite (**Figure 6D**). The results showed a significant decrease in the dendritic
258 I_A gradient in Cav2.3 KO neurons (**Figure 6E**). These findings suggest that Cav2.3 channel
259 expression is linked to maintenance of the magnitude of I_A in distal dendrites.
260
261 **Cav2.3 channels promote I_A-mediated excitatory synaptic filtering.**
262 Voltage-gated ion channels open in response to synaptic depolarization in excitatory
263 synapses (9, 55, 76, 77). Therefore, the size of the synaptic current measured at the cell soma is
264 not only the result of transmitter release and glutamate receptor function but also of active
265 membrane properties. Kv4.2 and Cav2.3 channels are localized to CA1 spines and dendrites
266 where they affect the synaptic potential and shape its propagation (5, 50, 51, 55, 78-80). We have
267 previously shown that I_A reduces the magnitude of spontaneous miniature EPSCs (81). Therefore,
268 if Cav2.3 channels boost I_A, Ni^{2+} would be expected to reduce I_A in spines and dendrites and
269 enhance mEPSC propagation. To test this, we applied Ni^{2+} while holding cultured neurons at -70
270 mV and recorded AMPAR-mediated mEPSCs in the presence of voltage-gated Na^+ and GABAR

271 blockers (**Figure 7A**). Ni^{2+} caused a rightward shift in the cumulative distribution of mEPSC
272 amplitudes, though with smaller effect than direct blockade of Kv4 with AmmTX3 (**Figure 7B**).
273 Simultaneous application of Ni^{2+} and AmmTX3 to the bath mimicked AmmTX3 alone, suggesting
274 that Kv4 channel block occluded any additive effect of Ni^{2+} on mEPSC amplitudes (**Figure 7B,C**).
275 Despite an increase on postsynaptic currents, Ni^{2+} reduced mEPSC frequency consistent with the
276 contribution of Ni^{2+}-sensitive presynaptic VGCCs to glutamate release in the hippocampus
277 (**Figure 7D**) (50, 73, 82).
278 We next sought a method to investigate the local spatiotemporal effects of the Cav2.3-
279 Kv4.2 complex on synaptic function. Fluorescent Ca^{2+} indicators are suited for visualization of
280 NMDAR Ca^{2+} entry in response to spontaneous, quantal glutamate release (83-85). We
281 transfected cultured hippocampal neurons with the genetically-encoded fluorescent Ca^{2+} indicator
282 GCaMP6f along with mCherry to illuminate dendrite morphology. We imaged spontaneous
283 NMDAR-mediated Ca^{2+} transients in Mg^{2+}-free extracellular solution containing TTX to block
284 action potential backpropagation, which would obscure spontaneous quantal NMDAR-mediated
285 Ca^{2+} entry. The frequency, amplitude, and duration of spontaneous Ca^{2+} transients were highly
286 variable both among and within individual spines, with some spines being completely inactive
287 during imaging trials (**Figure 8A**). The NMDAR blocker APV completely abolished Ca^{2+} transients
288 consistent with a requirement for spontaneous glutamate release onto NMDARs to initiate Ca^{2+}
289 influx (**Figure 8A,B**). Variability and low event frequency required identification of spines that were
290 active both before and after pharmacological treatments. AmmTX3 block of Kv4 channels did not
291 alter the amplitude of Ca^{2+} transients but did lengthen the event half-width suggesting that Kv4
292 channels oppose spine depolarization initiated by glutamate receptors (**Figure 8C**). Kv4 block
293 increased the integrated amount of Ca^{2+} entry (**Figure 8D**). As expected, Ni^{2+} reduced integrated
294 spine Ca^{2+} signals likely due to a combinatorial effect on Ni^{2+} sensitive pre- and postsynaptic
295 VGCCs (**Figure 8E**). To determine if Cav2.3 Ca^{2+} entry modulated the function of Kv4 channels,
296 we applied Ni^{2+} followed by addition of AmmTX3. Preapplication of Ni^{2+} occluded the AmmTX3-
297 induced increase of spine Ca^{2+} suggesting Cav2.3-mediated Ca^{2+} entry is required to maintain
298 spine repolarization by Kv4 channels (**Figure 8F**).
299
300
301
302
303
304

305 DISCUSSION

306

307 The present study was designed to both confirm and define the nature of a Cav2.3-Kv4.2
308 complex identified from a proteomic screen and to assess its functional consequences in CA1
309 pyramidal neurons. We show here that Cav2.3 and Kv4.2 colocalize within dendritic spines of
310 CA1 pyramidal neurons, likely within a 10 nm nanodomain at 1:1 stoichiometry as shown by FRET
311 microscopy in HEK293FT cells (**Figures 1,2**). Functionally, we found that the Cav2.3-Kv4.2
312 interaction increases Kv4.2 surface localization and contributes to maintenance of the dendritic
313 gradient of I_A in CA1 pyramidal neurons (**Figures 3-6**). Previous studies have demonstrated that
314 dendritic I_A regulates excitability, spine Ca^{2+} entry, back propagation of action potentials, plateau
315 potentials, synaptic plasticity, and hippocampus-dependent learning (86-88). In regulating the
316 magnitude of I_A as shown here, the Cav2.3-Kv4.2 complex therefore plays a fundamental role in
317 dendritic function. Consequently, Cav2.3-mediated Ca^{2+} entry would be expected to support the
318 many roles of dendritic I_A. Indeed, we found that Ni^{2+} occluded AmmTX3-mediated boosting of
319 spine Ca^{2+} signals and increased the amplitude of AMPAR-mediated mEPSCs (**Figures 7,8**).
320 Here we have corroborated and expanded upon the studies of Wang and colleagues who
321 first described a Kv4 and R-type Ca^{2+} channel functional interaction at CA1 synapses (50). They
322 demonstrated that block of R-type VGCCs using SNX-482 increased the amplitude of Schaffer
323 collateral evoked EPSPs. This effect was occluded by Kv4 block using the non-selective voltage-
324 gated K^+ channel blocker 4-AP, expression of a dominant negative Kv4.2 (W362F) subunit, or
325 KChIP sequestration with a pan-KChIP antibody in the patch pipette. Furthermore, internal 10
326 mM BAPTA occluded the effect of SNX-482, which, together with the reliance on KChIPs,
327 provided evidence for a small intermolecular distance ($\leq$ 50 μm) between the Ca^{2+} source and the
328 putative Kv4 channels. One potential criticism of this work was the reliance on SNX-482, which,
329 shortly thereafter, was found to be a potent Kv4 blocker with an IC_{50} ~10-fold greater for Kv4.3
330 than Cav2.3 (89, 90). However, SNX-482 inhibition of the predominant CA1 isoform, Kv4.2 is
331 much less pronounced and the EPSP boosting effect was repeated using Ni^{2+}, an alternative
332 VGCC blocker (50). Most importantly, the SNX-482 effect could not be reproduced in Cav2.3 KO
333 mice (79). Together with the evidence presented here, there is a strong argument that the SNX-
334 482 effects observed in the Wang et al studies were likely due to VGCC block and not off target
335 effects at Kv4 channels.
336 Here we describe a novel connection between the Cav2.3 and Kv4.2 pore-forming
337 subunits functionally impacting synaptic integration. Cav2.3 and Kv4.2 double immunogold
338 labeling was not seen within the PSD (**Figure 1E**), rather complexes were localized to peri- or

339 extrasynaptic domains in spines as described previously (51, 81). Furthermore, we found that
340 heterologously expressed Cav2.3 and Kv4.2, in the absence of coexpressed auxiliary subunits,
341 form a nanodomain signaling complex using C-YFP FRET microscopy (**Figure 3**). FRET can only
342 be measured when C- and YFP are within 10 nm and we estimate the diameter of the Kv4-KChIP
343 complex itself to be close to ~10 nm based on the Kv2.1-β_2 channel structure (91). Therefore,
344 KChIPs arrayed around the intracellular T1 domain of the Kv4.2 channel could be exposed to
345 Ca^{2+} concentrations approaching 10 μM during Cav2.3 channel openings based on Ca^{2+} source
346 diffusion models (68). While the steady-state Ca^{2+} occupancy of KChIP is unknown *in vivo*,
347 dynamic KChIP Ca^{2+} binding is a compelling mechanism that may account for Cav2.3-mediated
348 regulation of Kv4.2 surface expression through reduced channel turnover. In a test tube, Ca^{2+}
349 binds to KChIP at high (EF3 and EF4) and low affinity sites (EF2, preferring Mg^{2+} over Ca^{2+}) and
350 Ca^{2+} binding plays a critical role in KChIP folding and binding to Kv4 channels (31, 36, 37, 43). In
351 reported structures, only EF3 and EF4 of KChIP1 are Ca^{2+}-bound, whereas it has been
352 hypothesized that EF2 distortion by Kv4.3 N-terminal binding renders it unable to accommodate
353 Ca^{2+} (31, 92, 93). While these studies are informative there remains a relative dearth of
354 mechanistic detail for Ca^{2+} regulation of endogenous Kv4-KChIP complexes involving full length
355 proteins and functional channels. While an *in vivo* mechanism for dynamic KChIP-Ca^{2+} exchange
356 remains elusive, KChIP binds Ca^{2+} in the μM range, suggesting local Ca^{2+} elevations may induce
357 KChIP structural rearrangements that promote Kv4.2 surface expression.

358 To our knowledge, the contribution of voltage-gated channels to quantal NMDAR-
359 mediated Ca^{2+} signals is unprecedented. In prior studies, pharmacological block of either AMPAR
360 or voltage-gated channels had no measurable effect on quantal NMDAR-mediated Ca^{2+} transients
361 (94, 95). However, subthreshold synaptic depolarizations can activate voltage-gated channels
362 including R-, T-type, and A-type channels (5, 9, 55, 76, 77). Why did prior studies not find a
363 contribution of voltage-gated channels to the quantal NMDAR-mediated Ca^{2+} signals? We found
364 that if our data were treated similarly, by measuring the mean amplitudes across spines before
365 and after treatments, the large variability both between and among spines obscured any effect of
366 pharmacological manipulation of voltage-gated channels (data not shown). The effects of
367 pharmacological treatments were only apparent through repeated imaging of specific spines
368 before and after treatments. We also found that Kv4 channels in particular, regulated the duration
369 of spine Ca^{2+} events more so than amplitude, necessitating comparison of Ca^{2+} signal integrals.
370 A presynaptic effect of Ni^{2+} and/or AmmTX3 on neurotransmitter release might also produce the
371 changes in spine Ca^{2+} signals we observed. To address this, we recorded AMPAR-mediated
372 mEPSCs, and application of Ni^{2+} increased mEPSC amplitude despite a reduction in frequency.

373 Conversely, AmmTX3 increased amplitude and did not affect mEPSC frequency consistent with
374 prior studies that have ruled out a presynaptic role for Kv4.2 channels (50, 96).
375 In the present study, we report measurements of I_A in cultured neurons and hippocampal
376 slices to provide strong evidence for regulation of the magnitude of I_A by Cav2.3 channels. Cav2.3-
377 mediated Ca^{2+} entry was sufficient to increase Kv4.2 functional expression in a KChIP-dependent
378 manner in non-neuronal cells. We also show Cav2.3 regulation of neuronal I_A using VGCC
379 pharmacology and Cav2.3 KO mice. Several lines of evidence support a Cav2.3-mediated Ca^{2+}-
380 and KChIP-dependent trafficking mechanism as opposed to regulation of Kv4.2 conductance or
381 gating in CA1 pyramidal neurons. First, increased single channel conductance has ostensibly
382 been ruled out as a mechanism for the increase in Kv4 current density mediated by KChIPs (97,
383 98). However, it is yet to be determined if elevations of intracellular Ca^{2+} may regulate Kv4 single
384 channel conductance. Second, we reported previously that elevated intracellular Ca^{2+} led to an
385 increase in Kv4 current density without affecting classical KChIP-dependent processes including
386 inactivation gating (42). However, stoichiometric KChIP binding is expression dependent (99-101)
387 and we should point out here that if Ca^{2+} caused shifts in Kv4 binding affinity for KChIP this likely
388 would be overcome by the significant overexpression of KChIP relative to Kv4 in those studies
389 (~8:1 molar excess). Lastly, our surface biotinylation experiments shown here demonstrate
390 increased Kv4.2 surface localization by Cav2.3 coexpression, again without changes in channel
391 gating consistent with our previous report. Taken together, Cav2.3-Kv4 functional coupling in CA1
392 pyramidal neurons primarily increases the magnitude of Kv4.2 currents through enhanced surface
393 expression or stability. This is in contrast to the mechanism demonstrated for the Cav3-Kv4
394 channel complex in cerebellar interneurons which results in enhanced I_A via a shift in channel
395 availability to more negative potentials (48, 49). It remains to be determined what mediates the
396 disparate regulatory mechanisms in CA1 pyramidal neurons and cerebellar stellate cells.
397 I_A increases linearly ~5-fold on the distal apical dendrites 350 μm from the soma of CA1
398 pyramidal neurons (5). Curiously, histochemical measurements of Kv4.2 expression levels
399 suggest at most a 2-fold increase in expression along the proximal-distal extent of the stratum
400 radiatum (1, 59, 78, 102). A constellation of studies supports both auxiliary subunit and enzyme-
401 dependent pathways may underlie the disparity between Kv4.2 expression and function. The
402 DPP6 auxiliary subunit establishes the Kv4.2 functional gradient in CA1 pyramidal neurons
403 through enhanced surface expression, a shifted voltage-dependence of activation to more
404 hyperpolarized potentials, and while the mechanistic basis for this is still unclear, DPP6 clearly
405 mediates dendrite directed Kv4.2 trafficking and function in distal dendrites (15). Distal dendritic
406 I_A activates at more negative membrane potentials when compared to proximal or somatic I_A (5),

407 and this is reversed by activity of PKA, protein kinase C (PKC), or mitogen activated kinase
408 pathways (12, 103, 104). During induction of synaptic plasticity, Kv4.2 channels internalize in an
409 NMDAR- and Ca^{2+}-dependent manner by PKA phosphorylation at Ser522 (61, 81). Furthermore,
410 Kv4.2 surface expression is bidirectionally regulated by local signaling of the Ca^{2+}-activated
411 phosphatase calcineurin (CaN) and PKA through the postsynaptic scaffolding protein
412 AKAP79/150 (63). We recently reported a role for a proline isomerase, Pin1 in activity-dependent
413 downregulation of Kv4.2 function downstream of p38 phosphorylation of T607 (58). Thus,
414 differential localization of kinases and phosphatases along the proximal-distal axis of CA1
415 pyramidal neurons could underlie the I_A gradient and is an important topic for further study. It is
416 possible that Cav2.3 Ca^{2+} entry may impinge on these pathways in a Ca^{2+}-nanodomain fashion.
417 For example, AKAP79/150 localizes PKA and CaN for phospho-regulation of AMPAR and L-type
418 Ca^{2+} channels (105). Hypothetically, Cav2.3 Ca^{2+} entry could also drive activation of AKAP-
419 anchored CaN and dephosphorylate Kv4.2 channels, favoring surface expression. Finding the
420 mechanistic link between local Ca^{2+} influx and increased Kv4.2 surface expression is a goal for
421 future research.

422 KChIP heterogeneity is a largely unexplored area of research in CA1 pyramidal neurons.
423 Alternative splicing and variable start codons of the *KCNIP1-4* transcripts result in up to 17 distinct
424 KChIP isoforms with unique N-terminal domains. Variant KChIPs have been categorized based
425 on the tendency for the N-terminus to mediate membrane interactions (33). A subset of
426 "cytoplasmic" KChIP isoforms confer Ca^{2+} regulation onto Kv4.2 channel complexes, N-
427 myristoylated isoforms do not, and reversibly palmitoylated isoforms have mixed Ca^{2+} sensitivity
428 (42). Members of a fourth transmembrane class of KChIPs retain Kv4.2 complexes within the ER
429 and reduce Kv4.2 surface expression when compared with other KChIP isoforms (106). In
430 hippocampus, there is overlapping expression of both Ca^{2+} sensitive and Ca^{2+} insensitive KChIP
431 isoforms. Could differential subcellular targeting of KChIPs lead to increased Kv4.2 function in
432 distal dendrites? Perhaps membrane-anchored KChIPs, like the Kv4.2 suppressor KChIP4a, may
433 be restricted to soma and proximal dendrites. *KCNIP1-4* mRNAs have been detected in the CA1
434 neuropil, suggesting they may be locally translated (107, 108). Dendrite targeted *KCNIP* mRNAs
435 may also undergo alternative splicing for conditional or spatiotemporal modification of Kv4.2
436 function. In fact, a KChIP4bL to KChIP4a splicing shift occurs in postmortem brain tissue isolated
437 from Alzheimer's patients resulting in reduced functional I_A (109). It is also possible that KChIPs
438 may confer Ca^{2+} regulation to Kv4 channel complexes through a mechanism unrelated to direct
439 KChIP-Ca^{2+} binding. KChIP assembly with Kv4.2 is required for downregulation of Kv4.2 surface
440 expression in response to PKA Ser552 phosphorylation (110). Additionally, reduced Kv4 function

441 by arachidonic acid is also mediated by assembly with KChIPs (111). Thus, there may be
442 ultrastructural roles of KChIPs that augment Kv4.2 in such a way as to affect sensitivity to various
443 forms of regulation.

444 The majority of CA1 dendritic I_A is mediated by Kv4.2 subunits, ruling out a significant
445 contribution of other A-type channels that include Kv1 and Kv4 subtypes (13). Here, we show that
446 the functional I_A gradient is disrupted in the Cav2.3 KO mouse (**Figure 6D,E**). Others too have
447 found that Ni^{2+} sensitive VGCCs are a significant source of Ca^{2+} in dendrites and spines (9, 55,
448 76, 77). One compelling hypothesis, given the results presented here, is that tonic Cav2.3 activity
449 in distal dendrites sustains Kv4.2 functional expression. The increasing distal dendritic gradient
450 of Kv4.2 expression correlates with the ratio of excitatory and inhibitory synapses along the apical
451 dendrite layers of the hippocampus (112, 113). Therefore, ongoing low-level spontaneous
452 excitatory synaptic transmission and Cav2.3-mediated Ca^{2+} entry may maintain Kv4.2 expression
453 as a homeostatic mechanism to regulate local dendritic excitability. This mechanism could be
454 overridden by LTP-stimulated endocytosis of Kv4.2 driven by strong synaptic input in an NMDAR-
455 dependent mechanism like we have previously described (61, 81). This would fit with the reported
456 increase in excitability of dendritic segments containing potentiated synapses following Shaffer
457 Collateral-CA1 LTP (88). The findings reported here open up several avenues of research into
458 the function of the Cav2.3-Kv4.2 complex in dendrite function and plasticity; however, a lack of
459 Cav2.3 specific pharmacology without overlapping effects at Kv4 channels makes this work more
460 challenging. Future studies aimed toward identifying Cav2.3-Kv4.2 interaction domains could be
461 leveraged to disrupt the complex. This would be of significant utility to isolate functions unique to
462 the Cav2.3-Kv4.2 complex as opposed to their independent roles in the hippocampus.
463
464
465
466
467
468
469
470
471
472
473
474

475 MATERIALS AND METHODS

476

477 **Mammalian expression vectors**

478 Cav2.3-GFP was a generous gift from Ehud Isacoff, University of California Berkeley (114). The
479 SGFP2-N1 plasmid was generated by replacement of YFP in YFP-N1 using AgeI/BsrGI sites to
480 excise SGFP2 from pSGFP2-C1 (Dorus Gadella, Addgene 22881 (115)). Kv4.2-CFP, Kv4.2-YFP,
481 and Kv4.2-SGFP2 fusions were created by ligating the mouse Kv4.2 (CCDS29974.1) from Kv4.2-
482 GFP (81) into the CFP-N1 vector using SalI/BglII sites. YFP-Cav2.3 was generated by PCR
483 amplification of the human Cav2.3 (CCDS55664.1) coding sequence from Cav2.3-GFP using
484 BglII/HindIII sites for ligation into the YFP-C1 vector (performed by Bioinnovatise, Inc). Rat pCMV-
485 KChIP2c was generously provided by Henry Jerng and Paul Pfaffinger, Baylor College of
486 Medicine, Houston, TX. Ca^{2+}-dead KChIP2c was generated by site directed mutagenesis using
487 D->A mutations at position 1 of each of EF2,3, and 4 (Stratagene, QuikChange Site-Directed
488 Mutagenesis Kit). KChIP2c-CFP was generated by PCR amplification of the rat KChIP2c ORF
489 (NM_001033961.1) from pCMV-KChIP2c and subcloned into CFP-N1 using BglII/SalI sites.
490 AKAP79-YFP and PKARII-CFP were gifts from Mark L. Dell'Acqua, University of Colorado School
491 of Medicine, Aurora, CO. The CFP-18aa-YFP tandem fusion construct used for FRET efficiency
492 calibrations was a gift from Clemens Kaminski (University of Cambridge). GCaMP6f was a gift
493 from Douglas Kim & GENIE project (Addgene 40755 (116)). Human Kv4.2-Myc-DDK (Origene,
494 RC215266), ECFP-N1, EYFP-C1, EYFP-N1, and mCherry-N1 are commercially available
495 (Takara Bio).

496

497 **Antibodies**

498 *Guinea pig anti-Cav2.3* was a generous gift from Akos Kulik, University of Freiburg (51), 1:100 for
499 EM; 1:1000 for IHC; 1:5000 for WB. *Mouse anti-Kv4.2* (K57/1): NeuroMab 75-016, 1:25 for EM;
500 1:300 for IHC; 1:2000 for WB. *Mouse anti-Myc*, Millipore 05-419, 1:500 for ICC. *Alexa Fluor 488*
501 *goat anti-guinea pig*: ThermoFisher A11073, 1:800 for IHC. *Alexa Fluor 488 goat anti-rabbit*:
502 ThermoFisher A11008, 1:500 for ICC. *Alexa Fluor 555 goat anti-mouse*: ThermoFisher A21422,
503 1:800 for IHC. *Alexa Fluor 647 goat anti-mouse*: ThermoFisher A21236, 1:500 for ICC. *Alexa*
504 *Fluor 680 goat anti-mouse*: ThermoFisher A21057, 1:10,000 for WB. *IRDye 800CW goat anti-*
505 *rabbit*: Li-Cor Biosciences 926-32211, 1:5,000 for WB. *Rabbit anti-GFP*, ThermoFisher A11122,
506 1:500 for ICC; 1:3000 for WB

507

508 **Cell culture**

509 HEK293FT and COS7 cells were maintained in DMEM supplemented with 10% fetal bovine
510 serum (ThermoFisher, A3160501) and 2% penicillin/streptomycin (ThermoFisher, 15140122) at
511 37°C and 5.0% CO_2. Cells were passaged 2x weekly by seeding 0.5-1.0 x 10^6 cells into 10 cm
512 culture dishes (Corning). Cell lines were kept up to passage 20.
513
514 **Humane rodent care and use**
515 All protocols and procedures were approved by the National Institute for Child Health and Human
516 Development Animal Care and Use Committee. All mice were housed and bred in the Porter
517 Neuroscience Research Center animal facility at the National Institutes of Health in Bethesda,
518 MD. Rodents were maintained on a 12 h light/dark cycle with *ad libitum* access to rodent chow
519 and water. Cav2.3 KO mice used for hippocampal cultures and brain slice electrophysiology were
520 generously provided by Dr. Richard Miller, Northwestern University (75). Cav2.3 KOs were
521 maintained on a C57Bl/6J background. Age-matched wild-type C57Bl/6J mice (WT) were used
522 as controls. Rat hippocampal neuronal cultures were prepared with embryos collected from E18-
523 19 timed pregnant Sprague Dawley rats bred at Taconic Biosciences and housed at the NIH for
524 4-5 days prior to euthanasia.
525
526 **Primary culture of rodent hippocampal neurons**
527 Neuronal hippocampal cultures prepared from embryonic day 18-19 (E18) rodent embryos were
528 performed as reported previously (69). Female dams were euthanized using CO_2 asphyxiation
529 followed by guillotine decapitation. Embryos were rapidly dissected from the uterine horn,
530 decapitated with sharp scissors, and whole heads were placed in ice-cold dissection medium
531 (ThermoFisher, 1X HBSS (14185052), 1 mM sodium pyruvate (11360070), 10 mM HEPES
532 (15630080), and 30 mM Glucose). After peeling away overlying skin and bone with forceps, brains
533 were removed from the skull and placed into fresh dissection medium. Each hemisphere of the
534 cerebral cortex was bisected from the hindbrain and the hippocampus was then gently rolled away
535 and excised from the cerebral cortex and placed into fresh ice-cold dissection medium. Once all
536 tissue was collected, the dissection medium was replaced with 5 ml room temperature (RT)
537 papain solution (5 ml dissection solution w/ 1% DNase (Worthington, LK003170) and 1 vial 0.22
538 μm filtered Papain (Worthington, LK003176). After a 45 min RT incubation, tissue was washed
539 4x with prewarmed NB5 medium (5% FBS (Hyclone, SH30071.03), ThermoFisher: 1X
540 Neurobasal A (21103049), 2% Glutamax (35050061), and 2% B27 (17504044). Tissue was
541 dissociated by gentle trituration using a 5 ml plastic serological pipette, cells were filtered through
542 a 70 μm cell strainer (Corning, 352350) and pelleted at 1,000 rpm in a swinging bucket centrifuge

543 (Beckman Coulter Allegra™ 6R) for 5 min at RT. Cells were resuspended in 10 ml NB5, diluted
544 1:1 in 0.4% Trypan Blue Stain (ThermoFisher, 15250061) and counted with a hemocytometer.
545 Neurons were plated 125,000 (rat) or 175,000 (mouse)/well in a 12–well plate (Corning)
546 containing glass coverslips. 12 mm round Poly-D-lysine/laminin pre-coated glass coverslips
547 (Corning, 354087) were used for electrophysiology. For immunostaining and fluorescence
548 microscopy neurons were plated on in-house Poly-D-lysine/laminin coated 18 mm German glass
549 coverslips (Carolina Biological, 633013). Briefly, UV-sterilized coverslips were incubated
550 overnight in poly-D-lysine (Sigma, P7280-5MG) dissolved in 22 µm filter-sterilized borate buffer
551 (50 mM boric acid, 12.5 mM sodium borate, pH 8.5). The following day, coverslips were washed
552 using sterile water and coated with 0.01 mg/ml mouse Laminin (ThermoFisher, 23017015) in PBS
553 for 3 hrs. 24 hrs after seeding, NB5 was replaced with Neurobasal A (Invitrogen) supplemented
554 as above but without FBS and 1% Glutamax (NB0). Neurons were fed twice per week thereafter
555 by replacing 0.4 ml with 0.5 ml fresh NB0 per well.
556
557 **Hippocampus area CA1 double immunogold electron microscopy**
558 Animals used for postembedding, double-immunogold localization were prepared as described
559 previously (117). Briefly, two male, adult Sprague Dawley rats were perfused with phosphate
560 buffer, followed by perfusion with 4% paraformaldehyde + 0.5% glutaraldehyde in phosphate
561 buffer, and then the brains were vibratomed, cryoprotected in glycerol overnight, frozen in a Leica
562 EM CPC (Vienna, Austria), and embedded in Lowicryl HM-20 resin in a Leica AFS freeze-
563 substitution instrument. Thin sections were incubated in 0.1% sodium borohydride + 50 mM
564 glycine in Tris-buffered saline plus 0.1% Triton X-100 (TBST), then in 10% normal goat serum
565 (NGS) in TBST, and then with 2 primary antibodies together in 1% NGS/TBST (overnight); then
566 they were incubated with the 2 immunogold-conjugated secondary antibodies (5+15 nm; Ted
567 Pella, Redding, CA, USA) in 1% NGS in TBST with 0.5% polyethylene glycol (20,000 MW), and
568 stained with uranyl acetate and lead citrate. Controls on sections from the same two rats, labeled
569 with the 2 secondary antibodies but without the primary antibodies, showed only rare gold and no
570 colocalization.
571
572 **Native hippocampal co-immunoprecipitation assays**
573 We performed native co-IP experiments to confirm an interaction between endogenous Cav2.3
574 and Kv4.2 channel with male, 12-week-old wild type C57BL/6 or control Cav2.3-KO mouse
575 hippocampus. Brain hippocampal tissue were lysed in lysis buffer: 150 mM NaCl, 20 mM Tris-
576 HCl, 1% CHAPS and protease inhibitor mixture (Roche, USA) and incubated for 20 min on ice,

577 then sonicated 5 times for 5 s each. The lysate was centrifuged at 15,000 xg for 20 min at 4°C
578 and supernatants were incubated with anti-Cav2.3 (2 µg/500 µg protein) and guinea-pig IgG
579 (ThermoFisher Scientific) as nonspecific control. The mixture was then incubated and rotated at
580 4°C overnight. The antibody-antigen complex was adsorbed onto 50 µl of immobilized protein A
581 (ThermoFisher Scientific) and incubated and rotated for 2-3 h at 4 °C. The protein-bead mixtures
582 were washed 5x with lysis buffer. The beads were resuspended in SDS sample buffer
583 (ThermoFisher, NP0007) to elute bound proteins. Protein complexes were immunoblotted as
584 described below.
585
586 **COS7 cell surface biotinylation**
587 Biotinylation assays were performed as previously described (81). COS7 cells are our preferred
588 cell line for surface biotinylation because of a higher surface to volume ratio and slower dividing
589 time relative to HEK293 cells. COS7 cells were transfected with Kv4.2 and Cav2.3-GFP
590 constructs using X-tremegene 9 transfection reagent (Sigma-Aldrich, 06365779001) for 24-36 h;
591 the cells were rinsed with ice-cold PBS, and surface protein was biotinylated with 1.5 mg/ml sulfo-
592 NHS-SS-biotin reagent (ThermoFisher) in PBS for 30 min on ice. Unbound biotin was quenched
593 with cold 50 mM glycine in PBS. Cells were lysed with ice-cold lysis buffer: 150 mM NaCl, 20 mM
594 Tris-HCl, 1% CHAPS and protease inhibitor mixture (Roche Diagnostics), sonicated and
595 centrifuged at 12,000 g for 10 min. Cell lysates were incubated overnight at 4°C with immobilized-
596 Streptavidin agarose beads (ThermoFisher), and unbound protein was removed from the beads
597 with 5 washes in lysis buffer. The bound proteins were eluted with SDS sample buffer
598 (ThermoFisher, NP0007). Surface expressed and total proteins were immunoblotted as
599 described below.
600
601 **Western blots**
602 Sample proteins were separated on 3-8% Tris-acetate gels (ThermoFisher, EA03752) using SDS
603 buffer (ThermoFisher, NP0002) and electrophoresis chambers (ThermoFisher, El0001). Proteins
604 were transferred using electrophoretic chambers (Bio-Rad, 1703930) in a Tris based buffer
605 (ThermoFisher, NP0006) to PVDF membranes (Millipore, IPFL00010). Immunoblots were
606 blocked for 1 h at RT and probed using primary antibodies overnight at 4°C in Odyssey blocking
607 buffer (Li-Cor Biosciences). After washes, immunoblots were probed for 1 h at RT with secondary
608 antibodies conjugated to infrared dyes for detection using the Odyssey infrared imaging system
609 (LI-COR Biosciences, Lincoln, NE). Quantification of results was performed using Odyssey
610 software.

611 **Immunostaining**

612 *Brain slices:* Deeply anesthetized mice were transcardially perfused with ice-cold
613 paraformaldehyde (PFA) solution (4% PFA (Electron Microscopy Sciences, 15714-S), PBS, pH
614 7.4). Whole brains were dissected, post-fixed in 4% PFA for 4 h, and cryopreserved with
615 increasing concentrations of sucrose solutions (10, 20 and 30% for 4, 12, and 12-24 h
616 respectively). Cryopreserved brains were sectioned in a cryostat at 7 µm thickness (Histoserv,
617 Inc.) through the dorsal hippocampus beginning at -1.955 mm caudal to bregma and adhered to
618 microscope slides (Superfrost™ Plus, ThermoFisher, 1255015) and stored at -80°C. After thawing
619 at RT for 15 min, a circle was drawn with a pap pen around each section to create a hydrophobic
620 barrier. Sections were rehydrated using PBS for 5 min at RT and blocked for 1 h at RT (0.3%
621 Triton X-100, 1% normal goat serum, PBS, pH 7.3-7.4). Next, fresh blocking solution containing
622 primary antibodies was applied and incubated 24-48 h at 4°C in a closed, humidified box. Slides
623 were washed 4 x 15 min in PBS with agitation. Secondary antibody was applied in 0.2% Triton X-
624 100 PBS and sections were incubated while protected from light for 2 h at RT. Sections were
625 washed 4 x 15 min in PBS with agitation. Coverslips were mounted using a DAPI-containing
626 mounting medium (ProLong™ Gold Antifade, ThermoFisher, P36931).

627 *Cultured hippocampal neurons:* Primary neurons grown on glass coverslips were washed 1x with
628 PBS and fixed in PFA solution for 10 min at RT. Neurons were washed 3 x 5 min with PBS and
629 permeabilized using 0.2% Triton X-100 for 10 min at RT. After 3 x 1 min PBS washes, neurons
630 were blocked with 3% BSA dissolved in PBS overnight at 4°C and protected from light. Primary
631 antibodies were applied in 3% BSA PBS for 2 h at RT with gentle agitation. Neurons were washed
632 3 x 1 min in PBS and secondary antibodies dissolved in PBS were incubated for 1 h at RT with
633 gentle agitation and protected from light. After 3 x 1 min washes, coverslips were mounted face-
634 down on glass slides in mounting medium with DAPI (ProLong™ Gold Antifade, ThermoFisher,
635 P36931).

636

637 **Confocal fluorescence microscopy and analysis**

638 PFA-fixed neuronal cultures and mouse brain slices were imaged using a Zeiss 710 laser
639 scanning confocal microscope running Zen Black software (Zeiss Microscopy). Fluorescence was
640 acquired using 405/449 nm (DAPI), 488/515 nm (Alexa 488), and 633/670 (Alexa 647) nm laser
641 excitation/emission wavelengths. Hippocampal sections were imaged using a Zeiss 10x Plan-
642 Apochromat 10x/0.45NA air objective capturing 0.83 µm/pixel in *x* and *y* dimensions. Z-stacks
643 were 20.83 µm tall with a 5.21 µm step size. A Zeiss 63x Plan-Apochromat/1.4NA oil objective

644 was used for cultured neurons yielding 0.13 μm/pixel in *x* and *y* dimensions. Z-stacks were 3.36
645 μm tall using 0.42 μm z-steps, and max intensity projections were used for analysis. Analysis was
646 performed in ImageJ (NIH). Spine and dendrite fluorescence intensities were measured by
647 masking all clearly identifiable mushroom-shaped spines and adjacent dendrite segments from
648 which they projected. Spine/dendrite ratios were calculated from the mean spine and dendrite
649 shaft intensities from each cell.
650
651 **Live-cell FRET microscopy in HEK293FT cells**
652 *FRET Acquisition:* Cultured HEK293FT cells were trypsinized ≤ 2 min, counted, and 75,000 cells
653 were seeded onto uncoated 18 mm glass coverslips. After 24 h growth, cells were transfected
654 using OPTI-MEM serum free medium, X-tremeGene 9 (Sigma, 6365779001) and various
655 plasmids. Living cells were imaged in a Tyrode's salt solution (in mM: 135 NaCl, 5 KCl, 2 $CaCl_2$,
656 1 $MgCl_2$, 25 HEPES, 10 glucose, pH 7.4) at RT 24–48 h post-transfection. An Observer.Z1
657 microscope (Zeiss) with a 63x plan-apochromat, 1.4 NA oil objective (Zeiss), Lambda LS Xenon
658 Arc Lamp Light Source System (Sutter Instruments), AxioCam MRm camera (Zeiss), and Zen
659 Blue software (Zeiss) were used for image acquisition. Three-filter FRET images were captured
660 using appropriate filter cubes (Semrock) housed in the microscope turret. CFP cube: (Ex. 438/24
661 nm, Em. 483/32 nm, Di. 458 nm), YFP cube: (Ex. 500/24 nm, Em. 542/27 nm, Di. 520 nm), and
662 FRET cube: (Ex. 438/24 nm, Em. 542/27 nm, Di. 458 nm). ImageJ software (NIH) was used for
663 image processing and calculations of sensitized FRET efficiency were adapted from the method
664 of Clemens Kaminski (118) with more details provided below.

665 *FRET analysis:* CFP, YFP, and CFP-YFP rawFRET fluorescence were captured in
666 single *xy* planes using the following excitation and detection scheme:

667 CFP image: CFP excitation and CFP emission (CFP fluorescence intensity)

668 YFP image: YFP excitation and YFP emission (YFP fluorescence intensity)

669 rawFRET image: CFP excitation and YFP emission (uncorrected FRET fluorescence intensity)

670 Fluorescence background was estimated by measuring the mean pixel values for several images
671 captured in a cell-free section of the coverslip on the experimental day. After background
672 subtraction, fluorescence intensity in the rawFRET image was corrected for CFP bleed-through
673 and YFP cross-excitation. A significant percentage of the fluorescent signal in the rawFRET image

674 is not due to FRET, but instead results from spectral crosstalk that must be subtracted. A
675 percentage of fluorescence emission from CFP is present in the YFP emission bandpass of the
676 rawFRET image (CFP bleed-through). Conversely, YFP cross-excitation occurs when CFP
677 excitation bandpass in the rawFRET image leads to direct excitation of YFP. For each FRET pair,
678 CFP bleed-through and YFP cross-excitation in the rawFRET image was measured by expressing
679 either the CFP or YFP construct alone and determining the ratio of fluorescence intensity in the
680 rawFRET image divided by the fluorescence intensity in the CFP (donor emission ratio (DER) or
681 YFP (Acceptor emission ratio (AER)) image across many cells. Each FRET pair yields unique
682 spectral cross-talk that when subtracted from the rawFRET image, generates the true signal due
683 to CFP/YFP FRET, known here as corrected FRET (FRETc). The equation

684 $$FRETc = rawFRET - (DER \times CFP) - (AER \times YFP)$$

685 was used to determine the amount of FRET in each cell. Mean CFP, YFP, and raw FRET
686 fluorescence intensities were measured by mask analysis of regions enriched for the construct of
687 interest. For cells expressing 1:1 stoichiometry of CFP and YFP, apparent FRET efficiency values
688 were calculated from mean intensities and normalized to the fraction of acceptor molecules
689 undergoing FRET ($FRET\ EFF_A$) using the equation:

690 $$FRET\ EFF_A = \frac{FRETc}{AER \times YFP \times \beta}$$

691 where β is a factor relating spectral and excitation efficiencies of donor and acceptor molecules.
692 For experiments measuring the stoichiometry of CFP/YFP FRET pairs, cells were transfected with
693 various ratios of CFP and YFP cDNAs and imaged as above. In addition to measuring FRET
694 EFF_A, FRET EFF_D was calculated using the equation:

695 $$FRET\ EFF_D = \frac{FRETc\ \frac{\alpha}{DER}}{CFP + FRETc\frac{\alpha}{DER}}$$

696 where α relates the quantum yields and signal detection efficiencies between donor and
697 acceptors. The values for α and β were found using the method of Kaminski (118). Briefly, using
698 the wide-field microscopy system described above, transfection of a control CFP-YFP tandem
699 fusion construct consisting of CFP and YFP separated by an 18 amino acid linker

700 (GLRSRAQASNSAVEGSAM) with a predetermined FRET efficiency of 0.38 allows for
701 determination of α and β using the following equations:

702 $$\alpha = \frac{0.38}{1 - 0.38} \frac{DER \times CFP}{FRETc}$$

703 $$\beta = \frac{FRETc}{AER \times YFP \times 0.38}$$

704 Plotting either FRET EFF_A vs. CFP/YFP or FRET EFF_D vs. YFP/CFP gives a measure of
705 saturating FRET at either the acceptor or donor. The ratio of the maximum FRET value normalized
706 for acceptor or donor concentration approximates the stoichiometry of the interaction as described
707 by others (66, 119, 120).

708 **Fluorescence recovery after photobleaching (FRAP) microscopy**

709 *FRAP acquisition:* Fluorescence imaging was performed on a Zeiss 710 laser scanning confocal
710 microscope equipped with a 405-30 nm diode laser, tunable Argon laser, DPSS 561-10 nm laser,
711 and a Zeiss 63x Plan-Apochromat/1.4 NA oil objective. A stage insert incubation system was used
712 to maintain cells at 34°C. Samples were illuminated at low laser power (2.0-3.5%). Image
713 acquisition and ROI bleaching was driven by Zen Black software (Zeiss Microscopy). Images
714 were acquired at 4X zoom yielding 0.033 μm/pixel. Cells were imaged 24-48 hrs after transfection
715 in Tyrode's salt solution. For HEK293FT cells, 500,000 cells were seeded onto 25 mm coverslips
716 in 6-well cell culture dishes (Corning). After 24 h, cells were transfected with CFP, YFP, Kv4.2-
717 CFP, or YFP-Cav2.3 constructs using X-tremeGene 9 Transfection Reagent (Sigma-Aldrich,
718 06365779001). Samples were illuminated at low laser power with either 405 nm or 515 nm laser
719 excitation, PMT gain of 700, and at 0.5 Hz. Both CFP and YFP fluorescence were photobleached
720 within a 50 px^2 ROI using 8 iterations of the 405 nm laser at 100% power. For cultured neurons,
721 DIV12-13 neurons were transfected with Kv4.2-sGFP2 and mCherry using Lipofectamine 2000
722 Transfection Reagent (ThermoFisher, 52887). Samples were illuminated with 488 nm and 560
723 nm laser excitation, PMT gain of 700-750, and at 0.2 Hz. Kv4.2-SGFP2 fluorescence was
724 photobleached within a 30 px^2 ROI for dendrite shafts and a custom ROI matching the shape of
725 each spine. Both dendrite and spine photobleaching required 8 iterations of the 405 nm laser at
726 100% power.

727 *FRAP data analysis:* FRAP data was processed and analyzed as previously described
728 (121) using the double normalization method described by Phair and Misteli (122),
729

730 $$I_{norm} = \frac{ref_{pre} \times (I_{FRAP}(t) - I_{bkgd}(t))}{\left(I_{ref}(t) - I_{bkgd}(t)\right) \times frp_{pre}}$$

731

732 Where ref_{pre} and frp_{pre} are the background corrected means of the pre-bleach time
733 points from the reference and FRAP region intensity traces, respectively. $I_{FRAP}(t)$ is the
734 fluorescence intensity within the FRAP ROI, $I_{bkgd}(t)$ is a background intensity from an ROI
735 outside the cell, and $I_{ref}(t)$ is the reference intensity in an unbleached region of the cell to account
736 for photobleaching during acquisition. FRAP curves from individual ROIs were vetted for adequate
737 bleaching (≥ 50% post-bleach intensity compared to pre-bleach intensity) and stability of intensity
738 trace (e.g., traces with distortions due to cellular movement or stage-drift were discarded). After
739 screening, normalized curves were then scaled 0 to 1 and averaged. Standard deviation and
740 standard error of the mean were calculated. Averaged curves were fitted with a single-
741 exponential, $FRAP(t) = A \times (1 - e^{-\tau \times t})$, where A is the mobile fraction using GraphPad Prism
742 software.

743

744 **HEK293FT cell whole-cell voltage-clamp recordings**

745 HEK293FT cells were seeded onto 35 mm cell culture dishes at a concentration of 500 x 10^6 cells
746 per dish. After 16-24 h, cultures were transfected with various plasmids (1-2 μg). To each dish,
747 DNA was first mixed with 300 μl Opti-MEM Reduced Serum Medium (ThermoFisher, 31985070)
748 reduced serum medium. Next, 6 μl X-tremegene 9 DNA Transfection Reagent (Sigma-Aldrich,
749 06365779001) was added and incubated for 10 min at room temperature before dropwise addition
750 to cultures. On the day of recording (24-48 h after transfection), cultures were trypsinized for ≤ 2
751 min and seeded at low density onto glass coverslips and allowed to adhere ≥ 1 h. Coverslips
752 were then transferred to a recording chamber and superfused (1-2 ml min^{-1}) in 95% O_2, 5% CO_2
753 saturated extracellular solution (in mM: 115 NaCl, 2.5 KCl,1.25 NaH_2PO_4, 25 $NaHCO_3$, 2 $CaCl_2$,
754 1 $MgCl_2$, 25 glucose, pH 7.2-7.3; 300 mOsm/l) at RT. Borosilicate patch electrodes were pulled
755 using a two-stage pipette puller (Narishige PC-10) to a tip resistance of 2.5-4.0 MΩ. Patch
756 electrodes were filled with (in mM): 115 KCl, 10 NaCl, 20 KOH, 10 Hepes, 10 EGTA, and 25
757 glucose (pH 7.3, 290 mOsm). Maximum voltage-gated K^+ currents were elicited by voltage steps
758 from a holding potential (-70 mV) to -120mV for 400 ms to relieve Kv4.2 channel inactivation and
759 to +60 mV for 400 ms to maximize channel opening. Inactivation rates were measured by fitting
760 the falling phase of macroscopic currents with a double exponential decay. Voltage dependence
761 of activation was performed using the same holding and hyperpolarizing steps as above but with

762 a range of intermediate activation potentials (-100, -80, -60, -40, -30, -20, -10, 0, +10, +20, +30,
763 +40, and +60 mV). Voltage-dependence of inactivation was determined using 400 ms conditioning
764 steps from holding to -140, -130, -120, -100, -80, -60, -40, -20, -10, and 0 mV immediately before
765 a 400 ms step to +60 mV. Recovery from inactivation was measured using two 400 ms voltage
766 steps to +60mV separated by various intervals (5, 10, 15, 20, 25, 50, 100, 200, and 500 ms).
767
768 **Cultured neuron whole-cell voltage-clamp recordings**
769 Primary hippocampal cultured neurons were grown on 12 mm coverslips to DIV6-9 for whole cell
770 recordings or DIV21-27 for miniature excitatory postsynaptic current recordings. At the time of
771 recording, a coverslip was transferred from a 12-well culture plate to the recording chamber and
772 superfused in extracellular solution as described above for HEK293FT cells. Patch electrodes
773 were pulled as described above to a tip resistance of 5-7 MΩ and back-filled with an internal
774 solution containing (in mM): 20 KCl, 125 K-gluconate, 5 EGTA, 4 NaCl, 4 Mg^{2+}-ATP, 0.3 Na-GTP,
775 10 HEPES, and 10 phosphocreatine (pH 7.2, 290 mOsm). Once whole-cell configuration was
776 achieved, neurons were held at -60 mV between voltage protocols. I_A was evoked with a 400 ms
777 conditioning step to -80 mV to relieve inactivation before stepping to 0 mV for 400 ms. I_A was
778 recorded in the presence of bath applied drugs to block contaminating postsynaptic currents: (in
779 μM) 0.5 Tetrodotoxin (TTX) (Tocris, 1069), 1.0 SR 95531 hydrobromide (Gabazine) (Tocris,
780 1262), 10.0 CNQX-Na^2 (Tocris, 1045), and 2.0 MK-801 maleate (Tocris, 0924). The voltage
781 protocol was repeated every 5 seconds for 6 min. Drugs were applied by rapid perfusion (3
782 ml/min) 20 sec after recordings began. IC_{50} for Ni^{2+} block of I_A was determined using a single
783 exponential fit to the dose-response curve. For measurements of the voltage-dependence of
784 inactivation, 400 ms conditioning steps from holding to -120, -100, -80, -70, -60, -50, -40, -20, -
785 10, and 0 mV immediately before a 400 ms step to 0 mV. Inactivation curves were fit to a
786 Boltzmann function. Miniature excitatory postsynaptic currents (mEPSCs) were recorded in the
787 presence of TTX and Gabazine. For mEPSC recordings in the presence of bath applied Ni^{2+} or
788 AmmTX3, a 10 min wash-in period ensured efficient R-current and I_A block, respectively before
789 patching. Immediately after break-in, mEPSCs were recorded in 2 min epochs at a holding
790 potential of -70 mV. Event amplitude was measured by the "Threshold Search" event detection
791 procedure in Clampfit. A maximum of 200 events from each neuron were included for analysis.
792
793 **Hippocampal slice preparation and CA1 pyramidal neuron recordings**
794 6-8 week-old male mice were anesthetized with isoflurane and decapitated. For cell-attached
795 dendritic recordings, mice were trans-cardially perfused with ice-cold slicing solution before

796 decapitation. Brains were then transferred into ice-cold slicing solution containing in mM: 2.5 KCl,
797 28 $NaHCO_3$, 1.25 NaH_2PO_4, 7 Glucose, 0.5 $CaCl_2$, 7 $MgCl_2$, 233 Sucrose, and bubbled with 95%
798 O2 / 5% CO2. Transverse slices of the hippocampus (300 µm) were made using a Leica VT1200S
799 vibrating microtome. Slices were transferred to 32ºC ACSF containing in mM: 125 NaCl, 2.5 KCl,
800 25 $NaHCO_3$, 1.25 NaH_2PO_4, 25 Glucose, 2$CaCl_2$, 1 $MgCl_2$, 1 ascorbic acid, 3 Na-Pyruvate, and
801 bubbled with 95% O2 / 5% CO2. After 25 minutes the slice chamber was transferred to room
802 temperature for the rest of the recording day. For recording, slices were transferred to a recording-
803 chamber with continuous flow of ACSF (2-3ml/min). Recording pipettes for somatic whole cell and
804 outside-out patch recordings had a tip-resistance of 3-5 MΩ and were filled with an internal
805 solution containing in mM: 20 KCl, 125 K-Gluconate, 1 EGTA, NaCl, 4 NaCl, Mg-ATP, 0.3 NaGTP,
806 10 HEPES, 10 Phosphocreatine, pH 7.26, 296 mOsm. Recording pipettes for dendritic cell-
807 attached voltage-clamp were filled with an internal solution mimicking ACSF, containing in mM: 3
808 KCl, 125 NaCl, 10 HEPES, 25 Glucose, 2$CaCl_2$, 1 $MgCl_2$, pH 7.24, 290 mOsm. Dendritic cell-
809 attached recordings were performed in voltage-clamp mode and voltage step protocols have been
810 inverted for readability in the results section, to account for the reversed polarity of the cell-
811 attached recordings. Protocols were designed for a theoretical resting membrane potential of -
812 60mV. I_A was calculated by subtracting I_{sus} from I_{tot}. I_{tot} was elicited using a voltage step to +40
813 from a -120 mV pre-pulse and a subsequent step to +40 from -30 mV was used to isolate I_{sus}.
814 Bath ACSF was supplemented with 1µM TTX to block voltage-gated sodium channels, 1µM
815 Gabazine to selectively block GABAA receptors, and 10µM CNQX to block AMPA-type and
816 Kainate-type glutamate receptors. Recording electrodes were pulled to 10-12 MΩ using a
817 Narishige PC-10 pipette puller and polished using a Narishige microforge.
818
819 **Electrophysiology equipment, data processing, and analysis**
820 Manual patch clamp experiments were performed on an Axioskop 2 FS Plus microscope (Zeiss)
821 with CP-Achromat 10× 0.25 air (Zeiss) and LumplanFL 60× 1.0 NA water immersion (Olympus)
822 objectives, and Sutter MPC-200 multi manipulator system with ROE-200 controller. The rig was
823 equipped with a Sutter LB-LS/17 lamp for fluorescence and DIC optics. An Axon Multiclamp 700B
824 amplifier, Axon Digidata 1440A A/D converter,and PClamp software (Molecular, Devices,
825 Sunnyvale, CA) were used to acquire electrophysiological signals. Currents were normalized to
826 cell size using whole-cell capacitance upon cell break-in, and leak currents were subtracted using
827 a P/4 protocol. Data were analyzed using Microsoft Excel, MATLAB, IGOR Pro (WaveMetrics,
828 Lake Oswego, OR), and GraphPad Prism. Pooled data are presented as either bar graphs ± SEM
829 overlaid with individual data points or in tabular format ± SEM.

830

831 **Cultured hippocampal neuron Ca^{2+} imaging and analysis**

832 Fast confocal imaging was performed using a 25× 1.1 NA water immersion objective on an A1R
833 MP HD system (Nikon) coupled to a Retiga ELECTRO CCD camera (QImaging) used for sample
834 scanning. Time-series were captured at 15.3 Hz using a 6x zoom on a resonant scanner yielding
835 0.08 μm/pixel. Image acquisition was controlled by Elements software (Nikon) and analysis was
836 performed in ImageJ (NIH). DIV13-15 primary hippocampal neurons grown on 18 mm glass
837 coverslips were transfected 24-48 h before imaging using Lipofectamine 2000. Neurons were
838 transfected with the genetically encoded Ca^{2+} indicator GCaMP6f and mCherry as a marker of
839 neuronal morphology. Coverslips were transferred to a quick release magnetic imaging chamber
840 (Warner, QR-41LP) with constant perfusion (1-2 ml/min) of modified Tyrode's salt solution (3 mM
841 $CaCl_2$, 0 mM $MgCl_2$, 10 μM glycine, 0.5 μM TTX) at RT. Spine Ca^{2+} signals were analyzed by
842 drawing a mask over the spine of interest. Mean GCaMP6f fluorescence intensity was measured
843 using the "Plot Z-axis Profile" function in imageJ. Extracted intensity values were background
844 subtracted and normalized to baseline fluorescence intensity ($\Delta F/F_0$). Only a transient > 2.5 fold
845 above baseline was used for analysis. Many of the analyzed Ca^{2+} transients were clearly
846 individual events; however, if two or more transients overlapped, we developed rules to discern
847 whether they should be considered multiple events. For a trailing event to be considered a unique
848 event, the first transient must have dropped >50% of maximum. Additionally, the trailing transient
849 must rise >50% above the lowest $\Delta F/F_0$ of the previous spike to be considered a separate event.
850 If a trailing transient did not meet both criteria it was not considered unique from the initiating
851 transient.

852
853
854
855
856
857
858
859
860
861
862
863

ACKNOWLEDGEMENTS

This work was supported by the Intramural Research Program of the Eunice Kennedy Shriver National Institute of Child Health and Human Development (J.G.M., J.J.G., L.L., J.H., and D.A.H.) and the National Institute of General Medical Sciences Postdoctoral Research Associate Training Grant (FI2 GM12004) (J.G.M.). Support was also provided by the Intramural Research Program of NIH/National Institute on Deafness and Other Communication Disorders (NIDCD) (Advanced Imaging Core-ZIC DC000081) (R.S.P. and Y-X.W.). We thank members of the Hoffman Lab for valuable discussions, protocols, and experimental assistance. We would like to thank Mark Dell'Acqua and for comments on this manuscript. We are grateful to Adriano Bellotti for contributing cultured rat neurons used in some experiments. The Ca^{2+}-dead KChIP2c construct was generated by site directed mutagenesis by Jung Park. Ying Liu bred, genotyped, and cared for the WT and Cav2.3 KO mice used in this work. We thank Vincent Schram (NICHD Microscopy & Imaging Core) for technical assistance.

COMPETING INTERESTS

Pertinent to contents of this manuscript, the authors have no competing financial or institutional interests to declare.

A

Protein	Number of peptides (Unique)	Number of peptides (Total)	% of aa sequence coverage
Kv4.2	96	386	67.30%
Kv4.1	21	35	31.07%
Kv4.3	25	33	37.56%
DPP6	7	8	9.78%
DPP10	2	2	2.14%
KChIP1	8	20	30.84%
KChIP2	7	8	27.04%
KChIP3	4	9	25.00%
KChIP4	8	16	33.20%

C

Position	Peptide	Δcorr	Xcorr
19-30	SLFIFGEDNIVR	0.148	2.48
352-362	NSGTSALEVLR	0.174	2.03
403-410	VDGASYFR	0.141	1.94
809-822	GDIGGLTSVLDNQR	0.345	2.9
1516-1528	LVNTSGFNMSFLK	0.052	2.19
1869-1884	ALPYLQQDPVSGLSGR	0.504	4.22
1938-1950	SNSSWLEEFSMER	0.402	2.76

B

Cav2.3 sequence:

```
1 malynpipvr qncftvnrsl fifgednivr kyakklidwp pfeymilati iancivlale 61
qhlpeddktp msrrlektep yfigifcfea gikivalgfi fhkgsylrng wnvmdfivvl 121
sgilatagth fnthvdlrtl ravrvlrplk lvsgipslqi vlksimkamv pllqigllll 181
failmfaiig lefysgklhr acfmnnsgil egfdpphpcg vqgcpagyec kdwigpndgi 241
tqfdnilfav ltvfqcitme gwttvlyntn dalgatwnwl yfipliiigs ffvlnlvlgv 301
lsgefakere rvenrrafmk lrrqqqiere lngyrawidk aeevmlaeen knsgtsalev 361
lrratikrsr teamtrdssd ehcvdissvg tplarasiks tkvdgasyfr hkerllrisi 421
rhmvksqvfy wivlsvvaln tacvaivhhn qpqwlthlly yaeflflglf llemslkmyg 481
mgprlyfhss fncfdfgvtv gsifevvwai frpgtsfgis vlralrllri fkitkywasl 541
rnlvvslmss mksiislflf lflfivvfal lgmqlfggrf nfndgtpsan fdtfpaaimt 601
vfqiltgedw nevmyngirs qggvssgmws aiyfivltlf gnytllnvfl aiavdnlana 661
qeltkdeqee eeafnqkhal qkakevspms apnmpsierd rrrrhhmsmw eprsshlrer 721
rrrhhmsvwe qrtsqlrrhm qmssqealnk eeappmnpln plnplsplnp lnahpslyrr 781
prpieglalg lglekceeer isrggslkgd iggltsvldn qrsplslgkr eppwlprsch 841
gncdptqqet gggetvvtfe drarhrqsqr rsrhrrvrte gkesasasrs rsasqersld 901
egvsidgeke hepqsshrsk eptiheeert qdlrrtnslm vprgsglvga ldeaetplvq 961
pqpelevgkd aalteqeaeg sseqalladv qldvgrgisq sepdlscmtt nmdkattest 1021
svtvaipdvd plvdstvvni snktdgeasp lkeaetkeee eevekkkqkk ekretgkamv 1081
phssmfifst tnpirkachy ivnlryfemc illviaassi alaaedpvlt nsernkvlry 1141
fdyvftgvft femvikmidq glilqdgsyf rdlwnildfv vvvgalvafa lanalgtnkg 1201
rdiktikslr vlrvlrplkt ikrlpklkav fdcvvtslkn vfnilivykl fmfifaviav 1261
qlfkgkffyc tdsskdteke cignyvdhek nkmevkgrew krhefhydni iwalltlftv 1321
stgegwpqvl qhsvdvteed rgpsrsnrme msifyvvyfv vfpfffvnif valiiitfqe 1381
qgdkmmeecs lekneracid faisakpltr ympqnrhtfq yrvwhfvvsp sfeytimami 1441
alntvvlmmk yysapwtyel alkylniaft mvfslecvlk viafgflnyf rdtwnifdfi 1501
tvigsiteii ltdsklvnts gfnmsflklf raarlikllr qgytirillw tfvqsfkalp 1561
yvclliamlf fiyaiigmqv fgnikldees hinrhnnfrs ffgslmllfr satgeawqei 1621
mlsclgekgc epdttapsgq nesercgtdl ayvyfvsfif fcsflmlnlf vavimdnfey 1681
ltrdssilgp hhldefvrvw aeydraacgr ihytemyeml tlmspplglg krcpskvayk 1741
rlvlmnmpva edmtvhftst lmalirtald ikiakggadr qqldselqke tlaiwphlsq 1801
kmldllvpmp kasdltvgki yaammimdyy kqskvkkqrq qleeqknapm fqrmepsslp 1861
qeiisnakal pylqqdpvsg lsgrsgypsm splspqeifq lacmdpaddg qfqeqqslvv 1921
tdpssmrrsf stirdkrsns swleefsmer ssentyksrr rsyhsslrls ahrlnsdsgh 1981
ksdthrsggr ergrskerkh llspdvsrcn seergtqadw esperrqsrs psegrsqtpn 2041
rqgtgslses sipsisdtst prrsrrqlpp vppkprplls ysslmrhtgg ispppdgseg 2101
gsplasqale snsacltess nslhpqqgqh pspqhyisep ylalhedsha sdcgeeetlt 2161
feaavatslg rsntigsapp lrhswqmpng hyrrrrlggl glammcgavs dllsdteedd 2221 kc
```

Figure 1 – Figure Supplement 1. A tandem affinity purification-mass spectrometry screen identifies Cav2.3 as a binding partner of Kv4.2.

A. The numbers of unique and total peptides, and the percent (%) amino acid sequence coverage for each protein that are presented in hippocampal neurons. **B.** Amino acid sequence coverage obtained for Cav2.3 protein from rat hippocampal neurons. Peptides detected by MS are underlined. **C.** Cav2.3 protein sequence report. Xcorr: Sequest cross-correlation score; Δcorr: Xcorr difference between the top ranked and next best sequence.

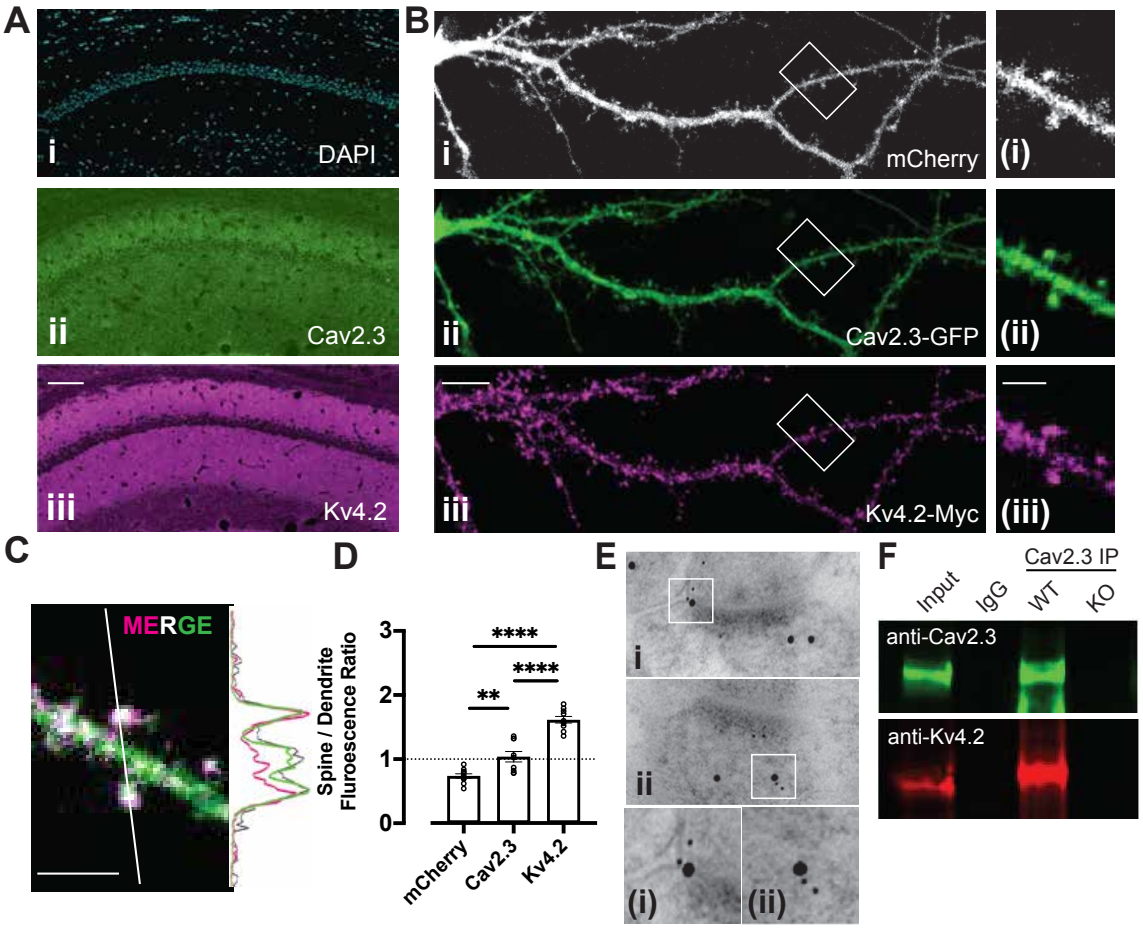

Figure 1. Cav2.3 and Kv4.2 colocalize in hippocampal neurons.

A. Mouse hippocampal brain sections were stained for (**Ai**) nuclei (DAPI), (**Aii**) Cav2.3, and (**Aii**) Kv4.2 channels. Cav2.3 and Kv4.2 are localized to dendrite fields of hippocampal area CA1. 100 μm scale bar **B.** Primary rat hippocampal neurons expressing (**Ai**, white) mCherry, (**Aii**, green) Cav2.3-GFP, and (**Aiii**, magenta) Kv4.2-myc. (Inset) Cav2.3 and Kv4.2 channel fluorescence is enriched in dendritic spines relative to mCherry. 10 μm and 3 μm scale bars **C.** Merged Kv4.2-myc and Cav2.3-GFP fluorescence of dendritic segment in panel **B**. The intensity profile demonstrates spine enrichment of both Cav2.3-GFP and Kv4.2-myc. 3 μm scale bar **D.** Cav2.3-GFP and Kv4.2-myc are enriched in spines when compared to cytosolic mCherry. n = 10; ** $p < 0.01$; **** $p < 0.0001$ by one-way ANOVA with Tukey's multiple comparison. **E.** Double immunogold electron micrographs of rat hippocampal sections labeled using 5 nm (Cav2.3) and 15 nm gold (Kv4.2). (insets) Cav2.3 and Kv4.2 colocalize within postsynaptic spines. **F.** Cav2.3 immunoprecipitation (green) pulls down Kv4.2 (red) from native hippocampal tissue.

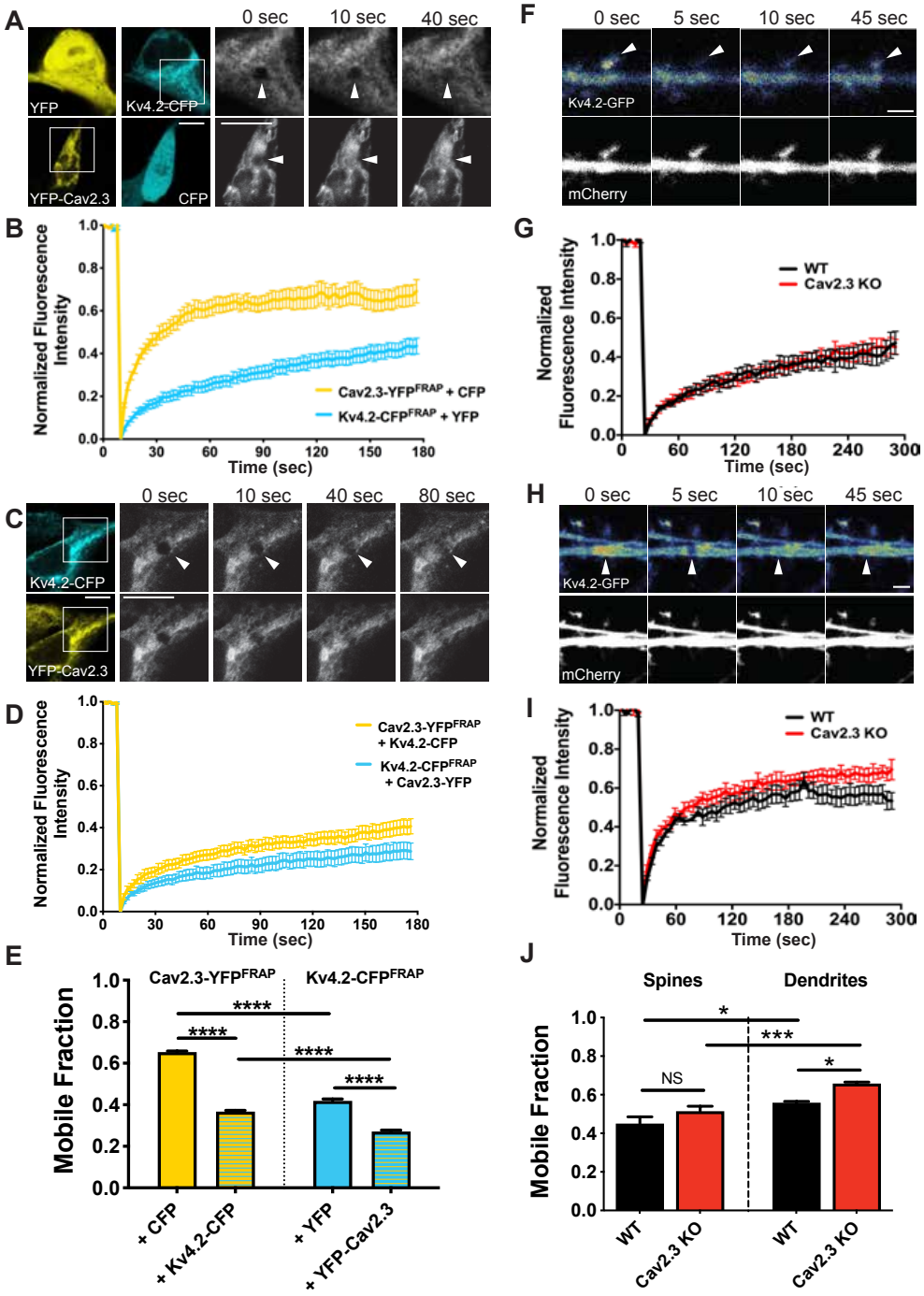

Figure 2. Cav2.3 regulates Kv4.2 mobility in HEK293FT cells and neuronal dendrites. **A.** HEK293FT cells were transfected with either YFP and Kv4.2-CFP (above) or YFP-Cav2.3 and CFP (below). FRAP time series for Kv4.2-CFP (above) or YFP-Cav2.3 (below) in gray scale. 5 μm scale bars. **B.** Fluorescence recovery within the bleached volume is plotted over time for Kv4.2-CFP and YFP-Cav2.3 when expressed with non-interacting fluorescent proteins (YFP and CFP, respectively). **C.** Representative images of coexpressed Kv4.2-CFP (above) and YFP-

935 Cav2.3 (below) and coincident FRAP time series are shown in gray scale. 5 μm scale bars. **D.**
936 FRAP recovery curves are plotted for coincident bleaching of Kv4.2-CFP and YFP-Cav2.3. **E.**
937 Averaged FRAP curves were fit with a single exponential and mobile fraction was plotted in bar
938 graphs for comparison among conditions. Coexpression of Kv4.2-CFP and YFP-Cav2.3 reduces
939 respective mobile fractions consistent with reciprocal interactions between the two channels. (n =
940 15-19 cells for each condition across 3 experiments) **F.** Dendrite Kv4.2-SGFP2 FRAP in a WT
941 mouse hippocampal neuron expressing Kv4.2-GFP (pseudocolor) and mCherry (white). 2 μm
942 scale bar. **G.** Dendrite Kv4.2-SGFP2 FRAP is plotted over time in WT (black) and Cav2.3 KO
943 mouse neurons (red). **H.** Spine Kv4.2-SGFP2 FRAP is shown as in F. 2 μm scale bar. **I.** Spine
944 Kv4.2-SGFP2 FRAP is plotted as in G. **J.** Bar graphs show mobile fraction extracted from single
945 exponential fits of averaged FRAP curves. Kv4.2-SGFP2 mobile fraction was significantly higher
946 in dendrites compared to spines. A larger Kv4.2-SGFP2 mobile fraction was detected in dendrites
947 of Cav2.3 KO mouse neurons when compared to WT. n = 17-18 spines and 14-17 dendrites from
948 7 WT and 7 Cav2.3 KO neurons. Data was pooled from 2-3 hippocampal cultures. Error bars
949 represent +/- SEM. * $p < 0.05$, *** $p < 0.001$, **** $p < 0.0001$. Statistical significance was
950 evaluated by one-way ANOVA with Tukey's multiple comparisons test.
951
952
953
954
955
956
957

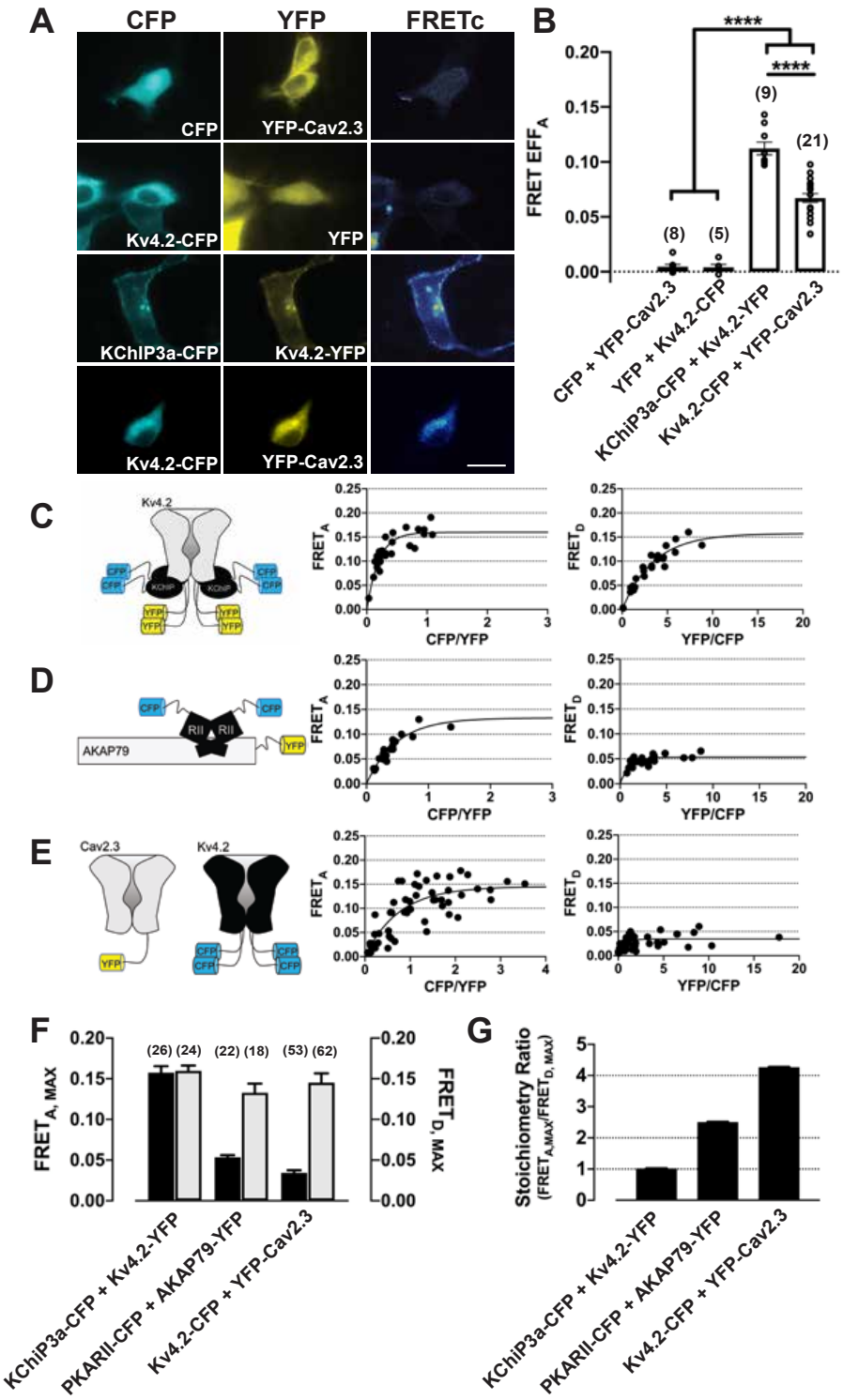

Figure 3. Cav2.3 and Kv4.2 bind at a 1:1 ion channel stoichiometry within a cellular nanodomain.

A. Representative raw CFP (cyan), YFP (yellow), and FRETc (pseudocolor) fluorescent images of HEK293FT cells expressing FRET constructs at equimolar concentrations. **B.** Bar graphs show

963 comparison of mean FRET efficiency normalized to acceptor concentration for each condition.
964 Parentheses indicate n values from 2-3 independent experiments. **C-E.** Left, cartoons depict the
965 expected stoichiometry of Kv4.2-YFP and KChIP2c-CFP (1:1) and AKAP79-YFP and PKARIIα-
966 CFP (1:2) while YFP-Cav2.3 and Kv4.2-CFP stoichiometry is inferred from the data. Right, cells
967 were transfected with various ratios of plasmid DNA. Donor and acceptor normalized FRET
968 efficiency were plotted for each cell over the ratio of donor and acceptor fluorescence. **F.** Bar
969 graphs compare acceptor (grey bars) and donor (black bars) normalized FRET efficiency for each
970 condition. Parentheses indicate n values from 2-3 biological replicates. **G.** FRET stoichiometry
971 ratio is calculated using the formula $FRET_{A,MAX}/\ FRET_{D,MAX}$ is plotted for FRET pairs confirming a
972 1:4 ratio of acceptor:donor or a 1:1 channel stoichiometry due to the tetrameric structure of Kv4.2.
973 Error bars represent +/- SEM. **** $p < 0.0001$. Statistical significance was evaluated by one-way
974 ANOVA with Tukey's multiple comparisons test.
975
976

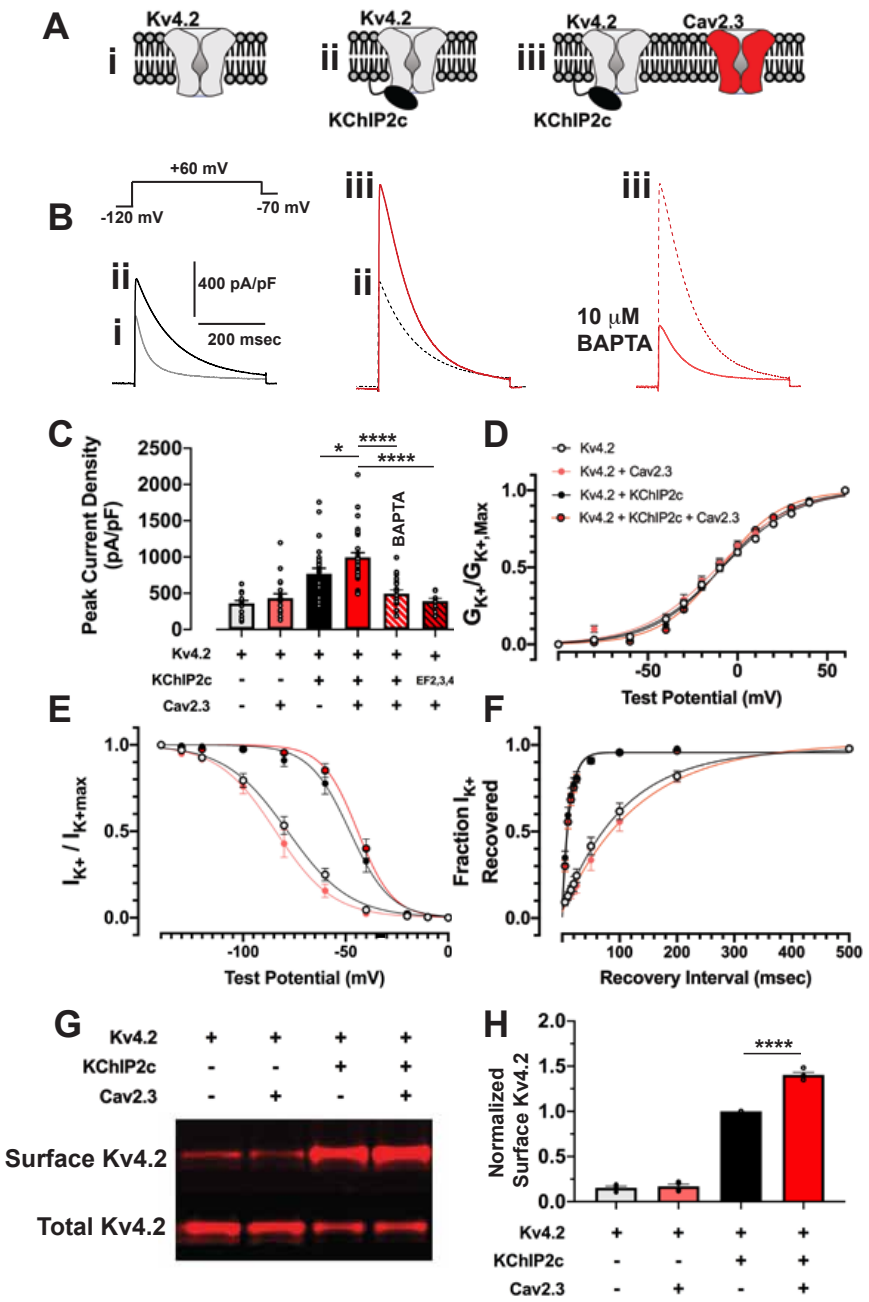

977

978 **Figure 4. Cav2.3 expression increases Kv4.2 current density in a KChIP- and Ca^{2+}-**
979 **dependent manner in HEK293FT cells.**

980 **A.** Cartoons depict a subset of transfection conditions with either Kv4.2 alone (**i**), Kv4.2 and
981 KChIP2c (**ii**), or Kv4.2, KChIP2c, and Cav2.3 (**iii**). **B.** Representative traces from conditions
982 shown in A. **C.** Bar graphs plot peak Kv4.2 current density under the conditions shown, n = 10-32
983 cells. Cav2.3 expression increases Kv4.2 current density in a KChIP-dependent manner, which
984 is reversed by replacement of EGTA with BAPTA in the patch pipette and by coexpression of EF-
985 dead KChIP2c. **D.** Kv4.2 voltage-dependence of activation is plotted using normalized

986 conductance against a range of membrane test potentials and fit to a Boltzmann function. **E.** Kv4.2
987 voltage-dependance of inactivation is plotted using normalized current against conditioning test
988 potentials and fit to a Boltzmann function. **F.** Kv4.2 recovery from inactivation is plotted as the
989 fraction of current recovered using a +60 mV test potential from an initial test potential of the same
990 magnitude against various recovery intervals. **G.** Representative western blot of a surface
991 biotinylation assay in COS7 cells transfected according to the indicated conditions. **H.** Bar graph
992 shows Kv4.2 surface expression normalized by day of experiment to the Kv4.2 and KChIP2c
993 expression condition. Error bars represent +/- SEM from 4 biological replicates. *$p < 0.05$, **** $p <$
994 0.0001. Statistical significance was evaluated by one-way ANOVA with Tukey's multiple
995 comparisons test.
996
997
998
999

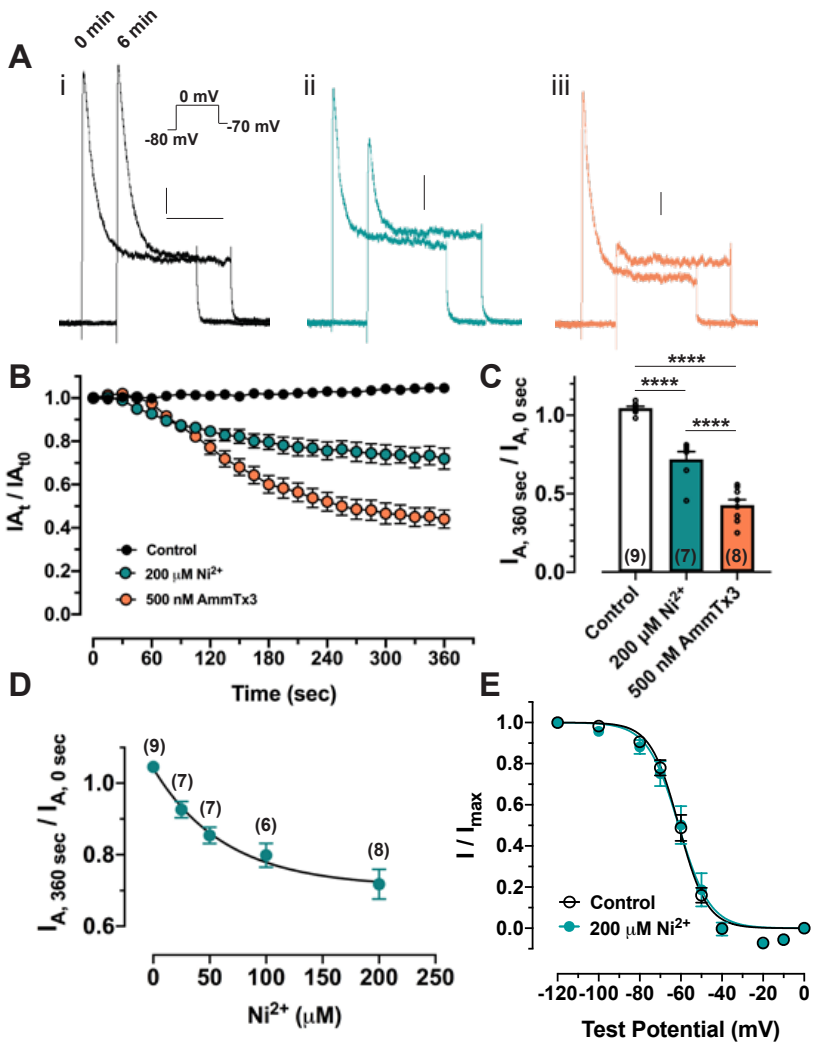

Figure 5. Cav2.3 sustains I_A in cultured hippocampal neurons.

A. Representative traces from whole-cell voltage clamp time courses for untreated neurons (i), and those treated with either Ni^{2+} (ii, 200 μM) or AmmTx3 (iii, 500 nM). First and last traces in the 6 min time course are shown superimposed with the final trace nudged 100 ms to the right. y-scale = 200 pA, x-scale = 200 ms. **B.** Averaged peak outward current normalized to current at break-in is plotted against the duration of the experiment. Drug wash-in began at 15 s. **C.** Outward current remaining at the end of the recording period was normalized to current at break-in and plotted for each condition. Cell numbers from 1-2 cultures are indicated within parentheses. **D.** Reduction in outward current was plotted for a range of Ni^{2+} concentrations. Averages at each concentration of Ni^{2+} were fit to a single exponential function. Cell numbers from 2 cultures are indicated within parentheses. **E.** Voltage-dependence of inactivation is plotted as the peak outward current elicited from a range of conditioning test potentials. Error bars represent +/- SEM

of 4 (control) or 7 (Ni^{2+}) cells from 1 culture. **** $p < 0.0001$. Statistical significance was evaluated by one-way ANOVA with Tukey's multiple comparisons test.

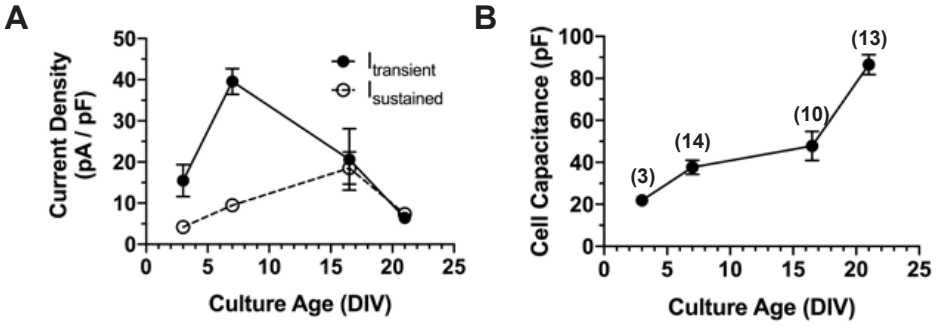

Figure 5 – Figure Supplement 1. Somatic I_A current density peaks early in developing cultured hippocampal neurons

A. Mean transient and sustained currents plotted by neuronal age in culture. **B.** Cell size measured by capacitance on break-in is plotted by neuronal age in culture. Number of cells are indicated in parentheses for **A** and **B**. Error bars represent +/- SEM from 1-2 cultures.

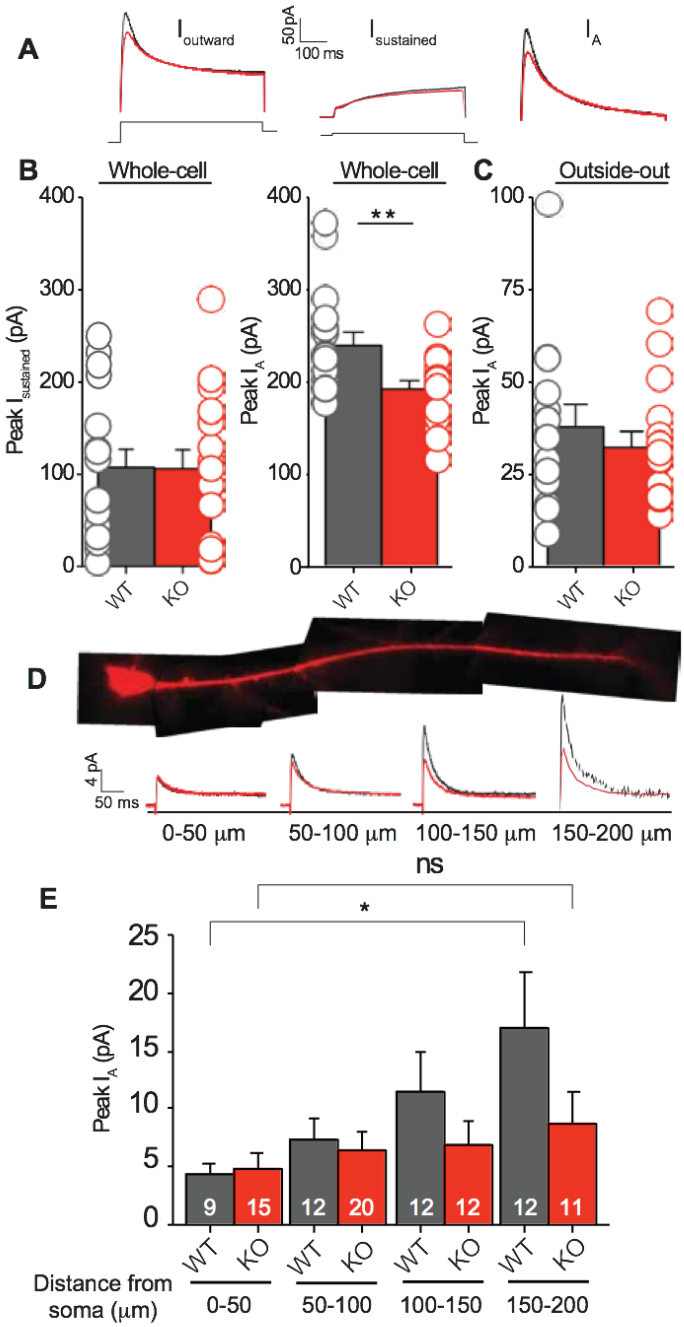

Figure 6. I_A is reduced in Cav2.3 KO CA1 pyramidal neurons.

A. Representative traces for total outward current, sustained current, and isolated I_A from the soma of WT or Cav2.3 KO mouse CA1 pyramidal neurons. **B.** Bar graphs compare the mean sustained and isolated I_A amplitude in WT and Cav2.3 KO mouse neuronal soma. n = 17 WT and 16 KO cells. **C.** Comparison of I_A in outside-out patches from the neuronal soma of WT and Cav2.3 KO. n = 14 WT and 15 KO cells. **D.** Above, a representative CA1 pyramidal neuron and apical dendrite made visible by Alexa 594 dye in the patch pipette. Below, representative cell-attached

recordings from the apical dendrites of WT and Cav2.3 KO neurons at various distances from the neuronal cell body. **E.** I_A is plotted for dendrite segments. The I_A gradient is dramatically reduced in Cav2.3 KO dendrites relative to WT. Parentheses indicate number of patches included in analysis. Error bars represent +/- SEM. ns = not statistically significant, * $p < 0.05$, ** $p < 0.01$. Statistical significance was evaluated by either student's t-test (**B**) or one-way ANOVA with Tukey's multiple comparisons test (**E**).

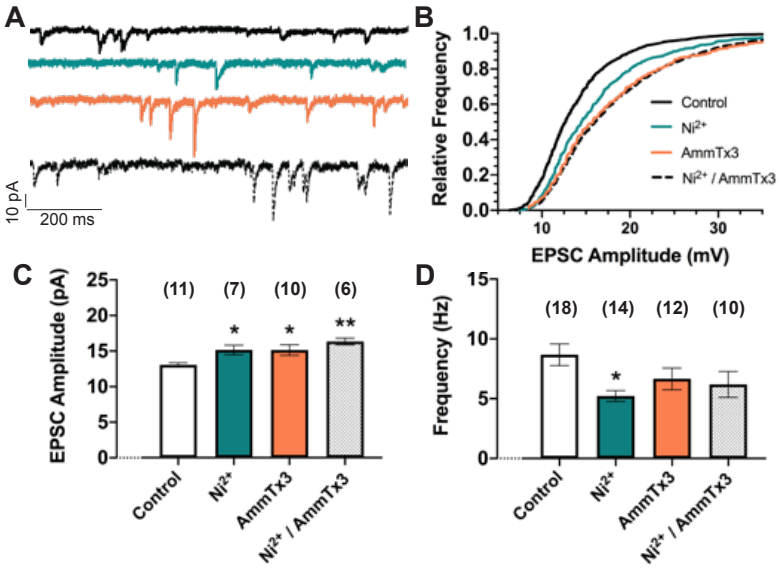

Figure 7. R-type Ca^{2+} channels regulate I_A attenuation of AMPAR-mediate mEPSCs.
A. Representative traces of miniature excitatory postsynaptic potentials measured from cultured hippocampal neurons at -70 mV in the absence and presence of Ni^{2+} or AmmTx3. **B.** The relative frequency distribution of mEPSCs are plotted against amplitude. Distribution of mEPSCs in the presence of Ni^{2+}, AmmTx3, or Ni^{2+} and AmmTx3 in combination are shifted toward a higher proportion of larger events. Analysis includes 638-1685 events **C.** Median mEPSC amplitudes are plotted for each condition recorded in **B**. Parentheses indicate cell numbers from 5 cultures. AmmTx3 increases median amplitude as does Ni^{2+} and AmmTx3 in combination. **D.** mEPSC frequency is decreased in the presence of Ni^{2+}, likely due to effects on presynaptic voltage-gated Ca^{2+} channels. Parentheses indicate cell numbers from 5 cultures. Error bars represent +/- SEM. * $p < 0.05$, ** $p < 0.01$. Statistical significance was evaluated by one-way ANOVA with Tukey's multiple comparisons test.

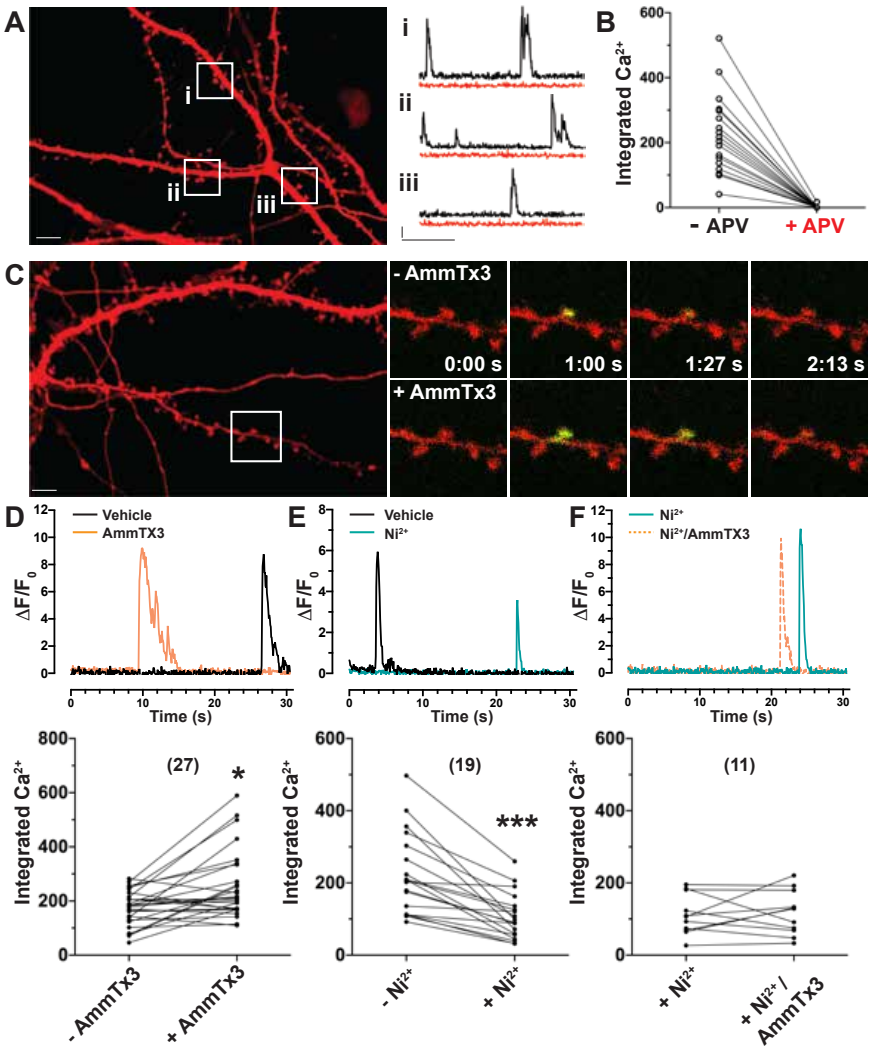

Figure 8. R-type Ca^{2+} channels regulate I_A attenuation of NMDAR-mediated spine Ca^{2+} influx.

A. Left, A representative neuron expressing mCherry (red) and GCaMP6f (not shown). Three representative spines (i, ii, and iii) were chosen to demonstrate typical spontaneous spine Ca^{2+} transients in the panel at right. Scale bar: 5 μm. Right, Traces plot the magnitude of GCaMP6f fluorescence ($\Delta F/F_0$) over time for each representative spine before (black traces) and after a 10 min application of D-APV (50 μM) (red traces). Scale bar: y = 2 $\Delta F/F_0$; x = 10 s. **B.** The integral of each Ca^{2+} transient for many spines is plotted before and after application of D-APV application demonstrating the NMDAR-dependence under these conditions. **C.** Left, A neuron transfected as in A, but treated with the Kv4 channel antagonist AmmTx3 (500 nM). Right, timelapse images of a representative spine before (above) and after (below) AmmTx3 treatment. **D.** Above, the magnitude of GCaMP6f fluorescence ($\Delta F/F_0$) over time in a single representative spine is plotted

1067 for each drug treatment. Below, integrated Ca^{2+} influx is plotted for many spines before and after
1068 the indicated conditions. Spine numbers from 2-4 cultures are indicated in parentheses. Only
1069 spines with at least one event before and after treatments were included in the analysis. * $p <$
1070 0.05, *** $p < 0.001$. Statistical significance was evaluated by two-way ANOVA with Sidak's
1071 multiple comparisons test.
1072
1073 REFERENCES
1074

1075 1. Maletic-Savatic M, Lenn NJ, Trimmer JS. Differential spatiotemporal expression of K+
1076 channel polypeptides in rat hippocampal neurons developing in situ and in vitro. J Neurosci.
1077 1995;15(5 Pt 2):3840-51.
1078 2. Sheng M, Tsaur ML, Jan YN, Jan LY. Subcellular segregation of two A-type K+ channel
1079 proteins in rat central neurons. Neuron. 1992;9(2):271-84.
1080 3. Serodio P, Rudy B. Differential expression of Kv4 K+ channel subunits mediating
1081 subthreshold transient K+ (A-type) currents in rat brain. J Neurophysiol. 1998;79(2):1081-91.
1082 4. Ramakers GM, Storm JF. A postsynaptic transient K(+) current modulated by arachidonic
1083 acid regulates synaptic integration and threshold for LTP induction in hippocampal pyramidal
1084 cells. Proc Natl Acad Sci U S A. 2002;99(15):10144-9.
1085 5. Hoffman DA, Magee JC, Colbert CM, Johnston D. K+ channel regulation of signal
1086 propagation in dendrites of hippocampal pyramidal neurons. Nature. 1997;387(6636):869-75.
1087 6. Gasparini S, Losonczy A, Chen X, Johnston D, Magee JC. Associative pairing enhances
1088 action potential back-propagation in radial oblique branches of CA1 pyramidal neurons. J
1089 Physiol. 2007;580(Pt.3):787-800.
1090 7. Cai X, Liang CW, Muralidharan S, Kao JP, Tang CM, Thompson SM. Unique roles of SK
1091 and Kv4.2 potassium channels in dendritic integration. Neuron. 2004;44(2):351-64.
1092 8. Kim J, Wei DS, Hoffman DA. Kv4 potassium channel subunits control action potential
1093 repolarization and frequency-dependent broadening in rat hippocampal CA1 pyramidal
1094 neurones. J Physiol. 2005;569(Pt 1):41-57.
1095 9. Seong HJ, Behnia R, Carter AG. Impact of subthreshold membrane potential on synaptic
1096 responses at dendritic spines of layer 5 pyramidal neurons in the prefrontal cortex. J
1097 Neurophysiol. 2014;111(10):1960-72.
1098 10. Cash S, Yuste R. Input summation by cultured pyramidal neurons is linear and position-
1099 independent. J Neurosci. 1998;18(1):10-5.
1100 11. Cash S, Yuste R. Linear summation of excitatory inputs by CA1 pyramidal neurons.
1101 Neuron. 1999;22(2):383-94.
1102 12. Watanabe S, Hoffman DA, Migliore M, Johnston D. Dendritic K+ channels contribute to
1103 spike-timing dependent long-term potentiation in hippocampal pyramidal neurons. Proc Natl
1104 Acad Sci U S A. 2002;99(12):8366-71.
1105 13. Chen X, Yuan LL, Zhao C, Birnbaum SG, Frick A, Jung WE, et al. Deletion of Kv4.2 gene
1106 eliminates dendritic A-type K+ current and enhances induction of long-term potentiation in
1107 hippocampal CA1 pyramidal neurons. J Neurosci. 2006;26(47):12143-51.

1108 14. Lockridge A, Yuan LL. Spatial learning deficits in mice lacking A-type K(+) channel
1109 subunits. Hippocampus. 2011;21(11):1152-6.
1110 15. Sun W, Maffie JK, Lin L, Petralia RS, Rudy B, Hoffman DA. DPP6 establishes the A-type
1111 K(+) current gradient critical for the regulation of dendritic excitability in CA1 hippocampal
1112 neurons. Neuron. 2011;71(6):1102-15.
1113 16. Wang HG, He XP, Li Q, Madison RD, Moore SD, McNamara JO, et al. The auxiliary subunit
1114 KChIP2 is an essential regulator of homeostatic excitability. J Biol Chem. 2013;288(19):13258-
1115 68.
1116 17. Andrasfalvy BK, Makara JK, Johnston D, Magee JC. Altered synaptic and non-synaptic
1117 properties of CA1 pyramidal neurons in Kv4.2 knockout mice. J Physiol. 2008;586(16):3881-92.
1118 18. Locke RE, Nerbonne JM. Role of voltage-gated K+ currents in mediating the regular-
1119 spiking phenotype of callosal-projecting rat visual cortical neurons. J Neurophysiol.
1120 1997;78(5):2321-35.
1121 19. Singh B, Ogiwara I, Kaneda M, Tokonami N, Mazaki E, Baba K, et al. A Kv4.2 truncation
1122 mutation in a patient with temporal lobe epilepsy. Neurobiol Dis. 2006;24(2):245-53.
1123 20. Gross C, Yao X, Engel T, Tiwari D, Xing L, Rowley S, et al. MicroRNA-Mediated
1124 Downregulation of the Potassium Channel Kv4.2 Contributes to Seizure Onset. Cell Rep.
1125 2016;17(1):37-45.
1126 21. Tiwari D, Brager DH, Rymer JK, Bunk AT, White AR, Elsayed NA, et al. MicroRNA
1127 inhibition upregulates hippocampal A-type potassium current and reduces seizure frequency in
1128 a mouse model of epilepsy. Neurobiol Dis. 2019;130:104508.
1129 22. Barnwell LF, Lugo JN, Lee WL, Willis SE, Gertz SJ, Hrachovy RA, et al. Kv4.2 knockout
1130 mice demonstrate increased susceptibility to convulsant stimulation. Epilepsia.
1131 2009;50(7):1741-51.
1132 23. Bernard C, Anderson A, Becker A, Poolos NP, Beck H, Johnston D. Acquired dendritic
1133 channelopathy in temporal lobe epilepsy. Science. 2004;305(5683):532-5.
1134 24. Monaghan MM, Menegola M, Vacher H, Rhodes KJ, Trimmer JS. Altered expression and
1135 localization of hippocampal A-type potassium channel subunits in the pilocarpine-induced
1136 model of temporal lobe epilepsy. Neuroscience. 2008;156(3):550-62.
1137 25. Hall AM, Throesch BT, Buckingham SC, Markwardt SJ, Peng Y, Wang Q, et al. Tau-
1138 dependent Kv4.2 depletion and dendritic hyperexcitability in a mouse model of Alzheimer's
1139 disease. J Neurosci. 2015;35(15):6221-30.
1140 26. Zemel BM, Ritter DM, Covarrubias M, Muqeem T. A-Type KV Channels in Dorsal Root
1141 Ganglion Neurons: Diversity, Function, and Dysfunction. Front Mol Neurosci. 2018;11:253.
1142 27. An WF, Bowlby MR, Betty M, Cao J, Ling HP, Mendoza G, et al. Modulation of A-type
1143 potassium channels by a family of calcium sensors. Nature. 2000;403(6769):553-6.
1144 28. Nadal MS, Ozaita A, Amarillo Y, Vega-Saenz de Miera E, Ma Y, Mo W, et al. The CD26-
1145 related dipeptidyl aminopeptidase-like protein DPPX is a critical component of neuronal A-type
1146 K+ channels. Neuron. 2003;37(3):449-61.
1147 29. Lin L, Sun W, Wikenheiser AM, Kung F, Hoffman DA. KChIP4a regulates Kv4.2 channel
1148 trafficking through PKA phosphorylation. Mol Cell Neurosci. 2010;43(3):315-25.
1149 30. Foeger NC, Marionneau C, Nerbonne JM. Co-assembly of Kv4 {alpha} subunits with K+
1150 channel-interacting protein 2 stabilizes protein expression and promotes surface retention of
1151 channel complexes. J Biol Chem. 2010;285(43):33413-22.

1152 31. Pioletti M, Findeisen F, Hura GL, Minor DL, Jr. Three-dimensional structure of the
1153 KChIP1-Kv4.3 T1 complex reveals a cross-shaped octamer. Nat Struct Mol Biol. 2006;13(11):987-
1154 95.
1155 32. Wang H, Yan Y, Liu Q, Huang Y, Shen Y, Chen L, et al. Structural basis for modulation of
1156 Kv4 K+ channels by auxiliary KChIP subunits. Nat Neurosci. 2007;10(1):32-9.
1157 33. Jerng HH, Pfaffinger PJ. Modulatory mechanisms and multiple functions of
1158 somatodendritic A-type K (+) channel auxiliary subunits. Front Cell Neurosci. 2014;8:82.
1159 34. Burgoyne RD. Neuronal calcium sensor proteins: generating diversity in neuronal Ca2+
1160 signalling. Nat Rev Neurosci. 2007;8(3):182-93.
1161 35. Lee L, Chen KC, Chang LS. Functional roles of EF-hands in human potassium channel-
1162 interacting protein 2.2. Protein Pept Lett. 2009;16(9):1081-7.
1163 36. Craig TA, Benson LM, Venyaminov SY, Klimtchuk ES, Bajzer Z, Prendergast FG, et al. The
1164 metal-binding properties of DREAM: evidence for calcium-mediated changes in DREAM
1165 structure. J Biol Chem. 2002;277(13):10955-66.
1166 37. Osawa M, Tong KI, Lilliehook C, Wasco W, Buxbaum JD, Cheng HY, et al. Calcium-
1167 regulated DNA binding and oligomerization of the neuronal calcium-sensing protein,
1168 calsenilin/DREAM/KChIP3. J Biol Chem. 2001;276(44):41005-13.
1169 38. Lin YL, Chen CY, Cheng CP, Chang LS. Protein-protein interactions of KChIP proteins and
1170 Kv4.2. Biochem Biophys Res Commun. 2004;321(3):606-10.
1171 39. Gonzalez WG, Pham K, Miksovska J. Modulation of the voltage-gated potassium channel
1172 (Kv4.3) and the auxiliary protein (KChIP3) interactions by the current activator NS5806. J Biol
1173 Chem. 2014;289(46):32201-13.
1174 40. Morohashi Y, Hatano N, Ohya S, Takikawa R, Watabiki T, Takasugi N, et al. Molecular
1175 cloning and characterization of CALP/KChIP4, a novel EF-hand protein interacting with
1176 presenilin 2 and voltage-gated potassium channel subunit Kv4. J Biol Chem.
1177 2002;277(17):14965-75.
1178 41. Groen C, Bahring R. Modulation of human Kv4.3/KChIP2 channel inactivation kinetics by
1179 cytoplasmic Ca(2). Pflugers Arch. 2017;469(11):1457-70.
1180 42. Murphy JG, Hoffman DA. A polybasic motif in alternatively spliced KChIP2 isoforms
1181 prevents Ca(2+) regulation of Kv4 channels. J Biol Chem. 2019;294(10):3683-95.
1182 43. Osawa M, Dace A, Tong KI, Valiveti A, Ikura M, Ames JB. Mg2+ and Ca2+ differentially
1183 regulate DNA binding and dimerization of DREAM. J Biol Chem. 2005;280(18):18008-14.
1184 44. Chen QX, Wong RK. Intracellular Ca2+ suppressed a transient potassium current in
1185 hippocampal neurons. J Neurosci. 1991;11(2):337-43.
1186 45. Wang X, Bao J, Zeng XM, Liu Z, Mei YA. Elevation of intracellular Ca2+ modulates A-
1187 currents in rat cerebellar granule neurons. J Neurosci Res. 2005;81(4):530-40.
1188 46. Patel SP, Campbell DL, Strauss HC. Elucidating KChIP effects on Kv4.3 inactivation and
1189 recovery kinetics with a minimal KChIP2 isoform. J Physiol. 2002;545(1):5-11.
1190 47. Vergara C, Latorre R, Marrion NV, Adelman JP. Calcium-activated potassium channels.
1191 Curr Opin Neurobiol. 1998;8(3):321-9.
1192 48. Anderson D, Rehak R, Hameed S, Mehaffey WH, Zamponi GW, Turner RW. Regulation of
1193 the KV4.2 complex by CaV3.1 calcium channels. Channels (Austin). 2010;4(3):163-7.
1194 49. Anderson D, Mehaffey WH, Iftinca M, Rehak R, Engbers JD, Hameed S, et al. Regulation
1195 of neuronal activity by Cav3-Kv4 channel signaling complexes. Nat Neurosci. 2010;13(3):333-7.

1196 50. Wang K, Lin MT, Adelman JP, Maylie J. Distinct Ca2+ sources in dendritic spines of
1197 hippocampal CA1 neurons couple to SK and Kv4 channels. Neuron. 2014;81(2):379-87.
1198 51. Parajuli LK, Nakajima C, Kulik A, Matsui K, Schneider T, Shigemoto R, et al. Quantitative
1199 regional and ultrastructural localization of the Ca(v)2.3 subunit of R-type calcium channel in
1200 mouse brain. J Neurosci. 2012;32(39):13555-67.
1201 52. Sabatini BL, Svoboda K. Analysis of calcium channels in single spines using optical
1202 fluctuation analysis. Nature. 2000;408(6812):589-93.
1203 53. Magee JC, Johnston D. Characterization of single voltage-gated Na+ and Ca2+ channels
1204 in apical dendrites of rat CA1 pyramidal neurons. J Physiol. 1995;487(1):67-90.
1205 54. Metz AE, Jarsky T, Martina M, Spruston N. R-type calcium channels contribute to
1206 afterdepolarization and bursting in hippocampal CA1 pyramidal neurons. J Neurosci.
1207 2005;25(24):5763-73.
1208 55. Bloodgood BL, Sabatini BL. Nonlinear regulation of unitary synaptic signals by CaV(2.3)
1209 voltage-sensitive calcium channels located in dendritic spines. Neuron. 2007;53(2):249-60.
1210 56. Takahashi H, Magee JC. Pathway interactions and synaptic plasticity in the dendritic tuft
1211 regions of CA1 pyramidal neurons. Neuron. 2009;62(1):102-11.
1212 57. Gutzmann JJ, Lin L, Hoffman DA. Functional Coupling of Cav2.3 and BK Potassium
1213 Channels Regulates Action Potential Repolarization and Short-Term Plasticity in the Mouse
1214 Hippocampus. Front Cell Neurosci. 2019;13:27.
1215 58. Hu JH, Malloy C, Tabor GT, Gutzmann JJ, Liu Y, Abebe D, et al. Activity-dependent
1216 isomerization of Kv4.2 by Pin1 regulates cognitive flexibility. Nat Commun. 2020;11(1):1567.
1217 59. Rhodes KJ, Carroll KI, Sung MA, Doliveira LC, Monaghan MM, Burke SL, et al. KChIPs and
1218 Kv4 alpha subunits as integral components of A-type potassium channels in mammalian brain. J
1219 Neurosci. 2004;24(36):7903-15.
1220 60. Wong W, Newell EW, Jugloff DG, Jones OT, Schlichter LC. Cell surface targeting and
1221 clustering interactions between heterologously expressed PSD-95 and the Shal voltage-gated
1222 potassium channel, Kv4.2. J Biol Chem. 2002;277(23):20423-30.
1223 61. Hammond RS, Lin L, Sidorov MS, Wikenheiser AM, Hoffman DA. Protein kinase a
1224 mediates activity-dependent Kv4.2 channel trafficking. J Neurosci. 2008;28(30):7513-9.
1225 62. Gardoni F, Mauceri D, Marcello E, Sala C, Di Luca M, Jeromin A. SAP97 directs the
1226 localization of Kv4.2 to spines in hippocampal neurons: regulation by CaMKII. J Biol Chem.
1227 2007;282(39):28691-9.
1228 63. Lin L, Sun W, Kung F, Dell'Acqua ML, Hoffman DA. AKAP79/150 impacts intrinsic
1229 excitability of hippocampal neurons through phospho-regulation of A-type K+ channel
1230 trafficking. J Neurosci. 2011;31(4):1323-32.
1231 64. Förster T. Zwischenmolekulare Energiewanderung und Fluoreszenz. Annalen der Physik.
1232 1948;437:55-75.
1233 65. Lakowicz JR. Principles of fluorescence spectroscopy. 3rd ed. New York: Springer; 2006.
1234 xxvi, 954 p. p.
1235 66. Ben-Johny M, Yue DN, Yue DT. Detecting stoichiometry of macromolecular complexes in
1236 live cells using FRET. Nat Commun. 2016;7:13709.
1237 67. Naraghi M, Neher E. Linearized buffered Ca2+ diffusion in microdomains and its
1238 implications for calculation of [Ca2+] at the mouth of a calcium channel. J Neurosci.
1239 1997;17(18):6961-73.

1240 68. Augustine GJ, Santamaria F, Tanaka K. Local calcium signaling in neurons. Neuron.
1241 2003;40(2):331-46.
1242 69. Gray EE, Murphy JG, Liu Y, Trang I, Tabor GT, Lin L, et al. Disruption of GpI mGluR-
1243 Dependent Cav2.3 Translation in a Mouse Model of Fragile X Syndrome. J Neurosci.
1244 2019;39(38):7453-64.
1245 70. Soong TW, Stea A, Hodson CD, Dubel SJ, Vincent SR, Snutch TP. Structure and functional
1246 expression of a member of the low voltage-activated calcium channel family. Science.
1247 1993;260(5111):1133-6.
1248 71. Maffie JK, Dvoretskova E, Bougis PE, Martin-Eauclaire MF, Rudy B. Dipeptidyl-peptidase-
1249 like-proteins confer high sensitivity to the scorpion toxin AmmTX3 to Kv4-mediated A-type K+
1250 channels. J Physiol. 2013;591(10):2419-27.
1251 72. Vacher H, Alami M, Crest M, Possani LD, Bougis PE, Martin-Eauclaire MF. Expanding the
1252 scorpion toxin alpha-KTX 15 family with AmmTX3 from Androctonus mauretanicus. Eur J
1253 Biochem. 2002;269(24):6037-41.
1254 73. Myoga MH, Regehr WG. Calcium microdomains near R-type calcium channels control
1255 the induction of presynaptic long-term potentiation at parallel fiber to purkinje cell synapses. J
1256 Neurosci. 2011;31(14):5235-43.
1257 74. Williams ME, Marubio LM, Deal CR, Hans M, Brust PF, Philipson LH, et al. Structure and
1258 functional characterization of neuronal alpha 1E calcium channel subtypes. J Biol Chem.
1259 1994;269(35):22347-57.
1260 75. Wilson SM, Toth PT, Oh SB, Gillard SE, Volsen S, Ren D, et al. The status of voltage-
1261 dependent calcium channels in alpha 1E knock-out mice. J Neurosci. 2000;20(23):8566-71.
1262 76. Magee JC, Christofi G, Miyakawa H, Christie B, Lasser-Ross N, Johnston D. Subthreshold
1263 synaptic activation of voltage-gated Ca2+ channels mediates a localized Ca2+ influx into the
1264 dendrites of hippocampal pyramidal neurons. J Neurophysiol. 1995;74(3):1335-42.
1265 77. Grunditz A, Holbro N, Tian L, Zuo Y, Oertner TG. Spine neck plasticity controls
1266 postsynaptic calcium signals through electrical compartmentalization. J Neurosci.
1267 2008;28(50):13457-66.
1268 78. Kerti K, Lorincz A, Nusser Z. Unique somato-dendritic distribution pattern of Kv4.2
1269 channels on hippocampal CA1 pyramidal cells. Eur J Neurosci. 2012;35(1):66-75.
1270 79. Wang K, Kelley MH, Wu WW, Adelman JP, Maylie J. Apamin Boosting of Synaptic
1271 Potentials in CaV2.3 R-Type Ca2+ Channel Null Mice. PLoS One. 2015;10(9):e0139332.
1272 80. Bloodgood BL, Giessel AJ, Sabatini BL. Biphasic synaptic Ca influx arising from
1273 compartmentalized electrical signals in dendritic spines. PLoS Biol. 2009;7(9):e1000190.
1274 81. Kim J, Jung S, Clemens A, Petralia R, Hoffman DA. Regulation of Dendritic Excitability by
1275 Activity-Dependent Trafficking of the A-Type K+ Channel Subunit Kv4.2 in Hippocampal
1276 Neurons. Neuron. 2007;54(6):933-47.
1277 82. Gasparini S, Kasyanov AM, Pietrobon D, Voronin LL, Cherubini E. Presynaptic R-type
1278 calcium channels contribute to fast excitatory synaptic transmission in the rat hippocampus. J
1279 Neurosci. 2001;21(22):8715-21.
1280 83. Sinnen BL, Bowen AB, Gibson ES, Kennedy MJ. Local and Use-Dependent Effects of beta-
1281 Amyloid Oligomers on NMDA Receptor Function Revealed by Optical Quantal Analysis. J
1282 Neurosci. 2016;36(45):11532-43.

1283 84. Murthy VN, Sejnowski TJ, Stevens CF. Dynamics of dendritic calcium transients evoked
1284 by quantal release at excitatory hippocampal synapses. Proc Natl Acad Sci U S A.
1285 2000;97(2):901-6.
1286 85. Reese AL, Kavalali ET. Spontaneous neurotransmission signals through store-driven
1287 Ca(2+) transients to maintain synaptic homeostasis. Elife. 2015;4.
1288 86. Shah MM, Hammond RS, Hoffman DA. Dendritic ion channel trafficking and plasticity.
1289 Trends Neurosci. 2010;33(7):307-16.
1290 87. Stuart G, Spruston N, Häusser M. Dendrites. Third edition. ed. Oxford ;: Oxford
1291 University Press; 2016. xxi, 714 pages p.
1292 88. Johnston D, Christie BR, Frick A, Gray R, Hoffman DA, Schexnayder LK, et al. Active
1293 dendrites, potassium channels and synaptic plasticity. Philos Trans R Soc Lond B Biol Sci.
1294 2003;358(1432):667-74.
1295 89. Kimm T, Bean BP. Inhibition of A-type potassium current by the peptide toxin SNX-482. J
1296 Neurosci. 2014;34(28):9182-9.
1297 90. Newcomb R, Szoke B, Palma A, Wang G, Chen X, Hopkins W, et al. Selective peptide
1298 antagonist of the class E calcium channel from the venom of the tarantula Hysterocrates gigas.
1299 Biochemistry. 1998;37(44):15353-62.
1300 91. Long SB, Campbell EB, Mackinnon R. Crystal structure of a mammalian voltage-
1301 dependent Shaker family K+ channel. Science. 2005;309(5736):897-903.
1302 92. Zhou W, Qian Y, Kunjilwar K, Pfaffinger PJ, Choe S. Structural insights into the functional
1303 interaction of KChIP1 with Shal-type K(+) channels. Neuron. 2004;41(4):573-86.
1304 93. Scannevin RH, Wang K, Jow F, Megules J, Kopsco DC, Edris W, et al. Two N-terminal
1305 domains of Kv4 K(+) channels regulate binding to and modulation by KChIP1. Neuron.
1306 2004;41(4):587-98.
1307 94. Walker AS, Neves G, Grillo F, Jackson RE, Rigby M, O'Donnell C, et al. Distance-
1308 dependent gradient in NMDAR-driven spine calcium signals along tapering dendrites. Proc Natl
1309 Acad Sci U S A. 2017;114(10):E1986-E95.
1310 95. Metzbower SR, Joo Y, Benavides DR, Blanpied TA. Properties of Individual Hippocampal
1311 Synapses Influencing NMDA-Receptor Activation by Spontaneous Neurotransmission. eNeuro.
1312 2019;6(3).
1313 96. Jung SC, Hoffman DA. Biphasic somatic A-type K channel downregulation mediates
1314 intrinsic plasticity in hippocampal CA1 pyramidal neurons. PLoS One. 2009;4(8):e6549.
1315 97. Holmqvist MH, Cao J, Hernandez-Pineda R, Jacobson MD, Carroll KI, Sung MA, et al.
1316 Elimination of fast inactivation in Kv4 A-type potassium channels by an auxiliary subunit
1317 domain. Proc Natl Acad Sci U S A. 2002;99(2):1035-40.
1318 98. Beck EJ, Bowlby M, An WF, Rhodes KJ, Covarrubias M. Remodelling inactivation gating of
1319 Kv4 channels by KChIP1, a small-molecular-weight calcium-binding protein. J Physiol.
1320 2002;538(Pt 3):691-706.
1321 99. Kunjilwar K, Qian Y, Pfaffinger PJ. Functional stoichiometry underlying KChIP regulation
1322 of Kv4.2 functional expression. J Neurochem. 2013;126(4):462-72.
1323 100. Zhou J, Tang Y, Zheng Q, Li M, Yuan T, Chen L, et al. Different KChIPs compete for
1324 heteromultimeric assembly with pore-forming Kv4 subunits. Biophys J. 2015;108(11):2658-69.

1325 101. Kitazawa M, Kubo Y, Nakajo K. The stoichiometry and biophysical properties of the Kv4
1326 potassium channel complex with K+ channel-interacting protein (KChIP) subunits are variable,
1327 depending on the relative expression level. J Biol Chem. 2014;289(25):17597-609.
1328 102. Varga AW, Anderson AE, Adams JP, Vogel H, Sweatt JD. Input-specific
1329 immunolocalization of differentially phosphorylated Kv4.2 in the mouse brain. Learn Mem.
1330 2000;7(5):321-32.
1331 103. Yuan LL, Adams JP, Swank M, Sweatt JD, Johnston D. Protein kinase modulation of
1332 dendritic K+ channels in hippocampus involves a mitogen-activated protein kinase pathway. J
1333 Neurosci. 2002;22(12):4860-8.
1334 104. Hoffman DA, Johnston D. Downregulation of transient K+ channels in dendrites of
1335 hippocampal CA1 pyramidal neurons by activation of PKA and PKC. J Neurosci.
1336 1998;18(10):3521-8.
1337 105. Patriarchi T, Buonarati OR, Hell JW. Postsynaptic localization and regulation of AMPA
1338 receptors and Cav1.2 by beta2 adrenergic receptor/PKA and Ca(2+)/CaMKII signaling. EMBO J.
1339 2018;37(20).
1340 106. Jerng HH, Pfaffinger PJ. Multiple Kv channel-interacting proteins contain an N-terminal
1341 transmembrane domain that regulates Kv4 channel trafficking and gating. J Biol Chem.
1342 2008;283(51):36046-59.
1343 107. Cajigas IJ, Tushev G, Will TJ, tom Dieck S, Fuerst N, Schuman EM. The local transcriptome
1344 in the synaptic neuropil revealed by deep sequencing and high-resolution imaging. Neuron.
1345 2012;74(3):453-66.
1346 108. Biever A, Glock C, Tushev G, Ciirdaeva E, Dalmay T, Langer JD, et al. Monosomes actively
1347 translate synaptic mRNAs in neuronal processes. Science. 2020;367(6477).
1348 109. Massone S, Vassallo I, Castelnuovo M, Fiorino G, Gatta E, Robello M, et al. RNA
1349 polymerase III drives alternative splicing of the potassium channel-interacting protein
1350 contributing to brain complexity and neurodegeneration. J Cell Biol. 2011;193(5):851-66.
1351 110. Schrader LA, Anderson AE, Mayne A, Pfaffinger PJ, Sweatt JD. PKA modulation of Kv4.2-
1352 encoded A-type potassium channels requires formation of a supramolecular complex. J
1353 Neurosci. 2002;22(23):10123-33.
1354 111. Holmqvist MH, Cao J, Knoppers MH, Jurman ME, Distefano PS, Rhodes KJ, et al. Kinetic
1355 modulation of Kv4-mediated A-current by arachidonic acid is dependent on potassium channel
1356 interacting proteins. J Neurosci. 2001;21(12):4154-61.
1357 112. Nicholson DA, Trana R, Katz Y, Kath WL, Spruston N, Geinisman Y. Distance-dependent
1358 differences in synapse number and AMPA receptor expression in hippocampal CA1 pyramidal
1359 neurons. Neuron. 2006;50(3):431-42.
1360 113. Megias M, Emri Z, Freund TF, Gulyas AI. Total number and distribution of inhibitory and
1361 excitatory synapses on hippocampal CA1 pyramidal cells. Neuroscience. 2001;102(3):527-40.
1362 114. Ulbrich MH, Isacoff EY. Subunit counting in membrane-bound proteins. Nat Methods.
1363 2007;4(4):319-21.
1364 115. Kremers GJ, Goedhart J, van den Heuvel DJ, Gerritsen HC, Gadella TW, Jr. Improved
1365 green and blue fluorescent proteins for expression in bacteria and mammalian cells.
1366 Biochemistry. 2007;46(12):3775-83.
1367 116. Chen TW, Wardill TJ, Sun Y, Pulver SR, Renninger SL, Baohan A, et al. Ultrasensitive
1368 fluorescent proteins for imaging neuronal activity. Nature. 2013;499(7458):295-300.

1369 117. Petralia RS, Wang YX, Hua F, Yi Z, Zhou A, Ge L, et al. Organization of NMDA receptors at
1370 extrasynaptic locations. Neuroscience. 2010;167(1):68-87.
1371 118. Kaminski CF, Rees EJ, Schierle GS. A quantitative protocol for intensity-based live cell
1372 FRET imaging. Methods Mol Biol. 2014;1076:445-54.
1373 119. Chen H, Puhl HL, 3rd, Koushik SV, Vogel SS, Ikeda SR. Measurement of FRET efficiency
1374 and ratio of donor to acceptor concentration in living cells. Biophys J. 2006;91(5):L39-41.
1375 120. Hoppe A, Christensen K, Swanson JA. Fluorescence resonance energy transfer-based
1376 stoichiometry in living cells. Biophys J. 2002;83(6):3652-64.
1377 121. Murphy JG, Crosby KC, Dittmer PJ, Sather WA, Dell'Acqua ML. AKAP79/150 recruits the
1378 transcription factor NFAT to regulate signaling to the nucleus by neuronal L-type Ca(2+)
1379 channels. Mol Biol Cell. 2019;30(14):1743-56.
1380 122. Phair RD, Misteli T. High mobility of proteins in the mammalian cell nucleus. Nature.
1381 2000;404(6778):604-9.
1382